TITLE: SNARE protein tomosyn regulates dense core vesicle composition but not exocytosis in mammalian neurons.

Authors:

Aygul Subkhangulova[1], Miguel A. Gonzalez-Lozano[2], Alexander J. A. Groffen[3], Jan R. T. van Weering[3], August B. Smit[2], Ruud F. Toonen[1], Matthijs Verhage[1,3]

Affiliations:

1 Department of Functional Genomics, Center for Neurogenomics and Cognitive Research (CNCR), Vrije Universiteit (VU) Amsterdam, Amsterdam, Netherlands

2 Department of Molecular and Cellular Neurobiology, Center for Neurogenomics and Cognitive Research (CNCR), Vrije Universiteit (VU) Amsterdam, Amsterdam, Netherlands

3 Department of Human Genetics, Center for Neurogenomics and Cognitive Research (CNCR), Amsterdam University Medical Center (UMC), Netherlands

Current affiliation of Miguel A. Gonzalez-Lozano: Department of Cell Biology, Harvard Medical School, Boston, MA, 02115, USA

Corresponding authors:

Aygul Subkhangulova
Department of Functional Genomics
Center for Neurogenomics and Cognitive Research (CNCR)
Vrije Universiteit, De Boelelaaan 1085
1081 HV Amsterdam, Netherlands
a.subkhangulova@vu.nl

Matthijs Verhage
Department of Functional Genomics
Center for Neurogenomics and Cognitive Research (CNCR)
Vrije Universiteit, De Boelelaaan 1085
1081 HV Amsterdam, Netherlands
m.verhage@vu.nl

Abstract

Tomosyn is a large, non-canonical SNARE protein proposed to act as a competitive inhibitor of SNARE complex formation in vesicle exocytosis. In the brain, tomosyn inhibits fusion of synaptic vesicles (SVs), whereas its role in the fusion of neuropeptide-containing dense core vesicles (DCVs) is unknown. Here, we addressed this question using a new mouse model allowing conditional deletion of tomosyn (*Stxbp5*) and its paralogue tomosyn-2 (*Stxbp5l*), and an assay that detects DCV exocytosis with single vesicle resolution in primary hippocampal neurons. Surprisingly, loss of both tomosyns did not affect DCV exocytosis but resulted in a strong reduction of intracellular levels of many DCV cargos, most prominently brain-derived neurotrophic factor (BDNF), granin VGF and prohormone convertase PCSK1. Reduced levels of DCV cargos were paralleled by decreased DCV size and impaired mRNA expression of the corresponding genes. We conclude that tomosyns regulate neuropeptide and neurotrophin secretion via control of DCV cargo production, and not at the step of cargo release. Our findings suggest a differential effect of tomosyn on the two main secretory pathways in mammalian neurons and argues against a conserved role of tomosyn as competitive inhibitor of SNARE complex formation.

Key words: tomosyn, SNARE, secretion, neuropeptides, dense core vesicle

Introduction

Brain activity relies on the precisely regulated secretion of different chemical messengers, and most neurons co-release multiple neurotransmitters (Nusbaum *et al*, 2017). Classical small-molecule neurotransmitters (e.g., glutamate, γ-aminobutyric acid) are released from synaptic vesicles (SV), whereas neuropeptides and neurotrophic factors are packaged in and secreted from dense core vesicles (DCV). Exocytosis of both types of vesicles requires an identical basic machinery consisting of SNARE proteins: syntaxin-1 and SNAP25 at the plasma membrane, and VAMP2 on the vesicle. The SNARE domains of these proteins form a tight complex that brings the two membranes together and drives vesicle fusion. In addition to the basic SNARE machinery, many other proteins participate in the fusion process (reviewed in (Südhof, 2013; Rizo & Xu, 2015), of which some are differentially required for SV and DCV exocytosis (Persoon *et al*, 2019; Moro *et al*, 2021). The differences in molecular machinery may explain why SV and DCV exocytosis is triggered upon different stimulation paradigms and at different locations within neurons (reviewed in (Zupanc, 1996; Scalettar, 2006).

Tomosyn (STXBP5) is a large, evolutionary conserved SNARE protein discovered as an interactor of syntaxin-1 in rat brain (Fujita *et al*, 1998; Masuda *et al*, 1998). Tomosyn is expressed in a wide range of specialized secretory cell types, such as neurons, platelets, and neuroendocrine cells, suggesting a fundamental role of tomosyn in regulated secretion. Mammals express a second tomosyn gene, *STXBP5L*, which encodes tomosyn-2 with a nearly 80% amino acid similarity (Groffen *et al*, 2005). The two genes have a partially overlapping expression pattern in mouse brain suggesting functional redundancy (Groffen *et al*, 2005; Barak *et al*, 2010). Mutations in both genes were found in patients with neurodevelopmental disorders, suggesting a role of tomosyns in human brain function (Matsunami *et al*, 2013; Cukier *et al*, 2014; De Rubeis *et al*, 2014; Kumar *et al*, 2015).

Tomosyn is comprised of a C-terminal SNARE domain and N-terminal WD40 repeats folded into two seven-bladed β-propellers. The SNARE-domain of tomosyn is homologous to the SNARE domain of VAMP2 and mediates binding to syntaxin-1 and SNAP25. The resulting complex is remarkably similar in structure and stability to the fusogenic complex of syntaxin-1/SNAP25 with VAMP2 (Pobbati *et al*, 2004). However, in contrast to VAMP2 and most other SNARE proteins, tomosyn does not contain a transmembrane anchor and therefore cannot drive membrane fusion. This feature led to a hypothesis that tomosyn functions as an inhibitor of fusion by competing with VAMP2 for binding to syntaxin-1/SNAP25 (Hatsuzawa *et al*, 2003). In support of this hypothesis, overexpression of tomosyn in neuroendocrine PC12 cells and adrenal chromaffin cells inhibits fusion of secretory vesicles (Fujita *et al*, 1998; Hatsuzawa *et al*, 2003; Yizhar *et al*, 2004), and, conversely, loss of tomosyn in nematode, fruit fly and mouse brain increases SV release probability and enhances synaptic transmission (Gracheva *et al*, 2006; McEwen *et al*, 2006; Chen *et al*, 2011; Sauvola *et al*, 2021; Sakisaka *et al*, 2008; Ben-Simon *et al*, 2015). In addition, loss of tomosyn in *C. elegans* augments neuropeptide secretion, as evidenced by decreased DCV abundance at synapses and increased accumulation of a DCV cargo in scavenger cells (Gracheva *et al*, 2007; Ch'ng *et al*, 2008). Together, these studies suggest an evolutionary conserved role of tomosyn as an inhibitor of secretory vesicle exocytosis.

However, several lines of evidence argue against this conclusion. First, rat sympathetic neurons show a decrease in neurotransmitter release upon depletion of tomosyn (Baba *et al*, 2005). Second, platelets from *Stxbp5*-null mice show severely reduced exocytosis of all types of secretory granules, which results in excessive bleeding and impaired thrombus formation *in vivo* (Zhu *et al*, 2014; Ye *et al*, 2014). Finally, loss of SRO7 and SRO77, two yeast orthologs of mammalian tomosyns, causes a strong defect in exocytosis of post-Golgi vesicles (Lehman *et al*, 1999). Collectively, these studies suggest a positive role of tomosyn and its yeast orthologs in exocytosis. Thus, despite the clear importance of tomosyn in regulated secretion, its role in this process remains controversial.

In the brain, the role of mammalian tomosyn has been studied with a focus on SV exocytosis, whereas its effect on DCV exocytosis is unknown. In this study, we addressed this question using a mouse model with the inducible loss of all tomosyn and tomosyn-2 isoforms and show that tomosyns do not affect neuronal DCV exocytosis but, paradoxically, regulate DCV composition and intracellular levels of brain-derived neurotrophic factor (BDNF) and many neuropeptides. Thus, tomosyns differentially modulate two regulated secretory pathways in neurons (secretion from SVs and DCVs) and have an additional role in the regulation of intracellular DCV cargo levels.

Results

To explore the role of tomosyn in neuronal secretion, we generated a new mouse model to allow conditional deletion of tomosyn (*Stxbp5*) and tomosyn-2 (*Stxbp5l*) (Figure 1 supplement 1). Primary hippocampal neurons isolated from these mice showed a complete loss of tomosyns expression when transduced with a lentivirus encoding *Cre*-recombinase, as shown by Western blot (WB) and immunocytochemistry (ICC). As wildtype (WT) control, we used neurons isolated from the same litter but expressing a defective *Cre*-recombinase that lacks the DNA-binding domain (ΔCre). Double knockout (DKO) neurons developed normally in culture and did not show any defects in neurite outgrowth and synapse formation as evidenced by normal dendrite length and density of synaptophysin puncta (Figure 1 supplement 1 D-G).

To examine DCV fusion, we used a modification of a validated reporter consisting of neuropeptide Y (NPY) fused to super-ecliptic pHluorin (Figure 1A, Figure 1 supplement 2) (Persoon *et al*, 2018; Nassal *et al*, 2022). When expressed in primary neurons, this reporter localized almost exclusively to DCVs, as indicated by its co-localization with endogenous DCV markers IA-2 and chromogranins (CHGA, CHGB) (Figure 1 Supplement 2). Fusion of labeled DCVs with the plasma membrane was stimulated by repetitive bursts of action potentials (50Hz) delivered to single neurons grown on glial micro-islands. As shown previously (Persoon *et al*, 2018; van Westen *et al*, 2021), this stimulation resulted in a steep accumulation of fusion events that plateaued shortly before the end of the stimulation (Figure 1B). Surprisingly, the total number of fusion events was similar between WT and DKO neurons, with a tendency (p=0.09) towards a decrease in DKO neurons (Figure 1C). However, the total intracellular pool of the DCV reporter, visualized by a short application of 50 mM NH_4Cl to neurons to dequench intravesicular NPY-pHluorin, was decreased by 28% in DKO neurons (Figure 1D). The released fraction, i.e. the number of fusion events normalized to the intracellular pool of vesicles, was nearly identical between WT and DKO neurons (Figure 1E). Also, the fluorescence peak of individual fusion events, an estimate of NPY loading per vesicle, was not affected by the loss of tomosyns (Figure 1F). Thus, tomosyns are dispensable for the fusion of neuronal DCVs but regulate intracellular levels of the DCV reporter.

Tomosyn was proposed to act as an inhibitor of vesicle fusion by competing with VAMP2 for the binding to syntaxin-1 and SNAP25. Hence, loss of tomosyns may result in the increased formation of ternary synaptic SNARE complexes consisting of syntaxin-1, SNAP25 and VAMP2, as was shown for tomosyn-deficient fly brains (Sauvola *et al*, 2021). We examined levels of the assembled complexes in DKO neurons by SDS-PAGE on non-boiled neuronal lysates, based on the fact that these complexes are resistant to SDS but are disassembled at temperatures higher than 60℃ (Hayashi *et al*, 1994; Otto *et al*, 1997) (Figure 1G). As expected, a band of approximately 80 kDa that corresponds to the ternary complexes was readily detected with a syntaxin-1 antibody in non-boiled lysates and absent in lysates heated at 95℃. No difference in the intensity of the 80 kDa band was observed between the genotypes. These data suggest that tomosyns do not interfere with the formation of syntaxin-1 containing synaptic SNARE complexes in cultured neurons. Interestingly, in addition to the 80 kDa band, non-boiled WT lysates showed a band of approximately 200 kDa, which was absent in DKO lysates and, therefore, likely represents a complex of tomosyn with syntaxin-1 and SNAP25, suggesting that

this complex is resistant to SDS *in vivo*. This 200 kDa complex was also detected in WT neurons with an antibody against tomosyn (Figure 1G).

Despite normal DCV exocytosis, intracellular levels of the DCV reporter were decreased in DKO neurons (Figure 1D). This decrease was also observed in tetrodotoxin (TTX)-silenced network cultures of DKO neurons that were not subjected to electric stimulation (Figure 1H-I). Activity of the synapsin promoter used to drive expression of the DCV reporter was not significantly altered in DKO neurons, as shown by normal expression of enhanced green fluorescent protein (EGFP) from the same promoter (Figure 1 supplement 3). These data suggest that the decreased levels of the DCV reporter are not caused by decreased transcriptional activity of the construct driving the reporter expression.

We next examined if endogenous DCV cargos are also affected by the loss of tomosyns. Levels of brain-derived neurotrophic factor (BDNF), one of the most common DCV cargos in excitatory hippocampal neurons (Dieni *et al*, 2012), were decreased by 47% in DKO neurons as shown by ICC (Figure 2A-B). Levels of IA-2 (PTPRN), a transmembrane DCV-resident protein commonly used as a DCV marker, were also lower, by 25%, in DKO neurons as indicated by ICC, and by approximately 50% as evidenced by WB analysis, which allows to distinguish a proteolytically processed (mature) form of IA-2 that runs at approximately 65 kDa (Hermel *et al*, 1999) (Figure 2C-E). The cellular distribution of the two DCV markers was similar between the genotypes, with a comparable reduction in somas and neurites of DKO neurons and no re-distribution between the two compartments as detected by ICC. Markers of lysosomes/late endosomes, LAMP1 and LIMP2, were not affected by the loss of tomosyns, as shown by ICC and WB (Figure 2 supplement 1). These data suggest that tomosyns regulate the number and/or composition of neuronal DCVs but not of other post-Golgi vesicles.

To analyze proteins affected by the loss of tomosyns in an unbiased manner, we compared the proteome of cultured WT and DKO neurons by mass spectrometry. We detected approximately 8500 proteins, of which around 3% were differentially expressed ($\log_2$ fold change threshold 0.3) (Figure 3A). Gene ontology (GO) analysis of the proteins decreased in DKO neurons indicated a rather selective downregulation of proteins related to the cytoskeleton and secretory granules (Figure 3B). Most of the up-regulated proteins were mitochondrial proteins. BDNF, along with the gene products of the perturbed genes (STXBP5 and STXBP5L), was detected only in WT but not in DKO neurons (Figure 3C). Other common DCV cargos were decreased to a various extent in DKO, among them: granins VGF and SCG2, cargo processing enzymes PCSK1 and CPE, and transmembrane DCV proteins IA-2 (PTPRN) and PAM (Figure 3D). In contrast to the DCV-resident proteins, SV proteins did not follow any general trend in DKO neurons: while some proteins (VGLUT2, GAD67) were strongly increased in DKO, others (e.g. SYT12 and SV2B) were reduced to a similar extent and many were not significantly altered. In conclusion, interfering with expression of both tomosyns leads to a reduction in the cellular levels of cytoskeletal and DCV cargo proteins and an increase in mitochondrial proteins.

Next, we examined ultrastructural morphology of DCVs in DKO and WT neurons by electron microscopy (Figure 4). We found DCVs with normal dense cores sparsely distributed among neurites in neurons of both genotypes. Most presynaptic sections did not contain any DCVs, in line with previous reports (Sorra *et al*, 2006; Persoon *et al*, 2018). Percent of synaptic sections

containing one or several DCVs was decreased in DKO by 30% (12% of all synaptic sections in DKO versus 17% in WT), indicating lowered DCV abundancy in DKO. In addition, DCVs in DKO neurons were slightly reduced in diameter (average 65.01 ± 2.08 nm in DKO versus 71.52 ± 1.62 nm in WT), with a high proportion of DKO DCVs being only 40-50 nm in diameter (16% of all DCVs in DKO versus 4% in WT) (Figure 4A-B). Such a reduction in diameter translates to an approximately 25% decrease in volume. In contrast, the diameter of SV was not affected by the loss of tomosyns (Figure 4D-E). Other parameters of synaptic ultrastructure, such as SV number per synapse, length of the active zone, and length of postsynaptic density, were also unchanged in DKO neurons (Figure 4D, 4F-H) and DKO somata showed no obvious abnormalities in organelle morphology (Figure 4D). Hence, loss of tomosyns leads to a specific reduction in DCV size and abundancy, without affecting ultrastructure and number of SVs.

The fact that abundancy, composition, and size of neuronal DCVs is affected in DKO neurons suggests that tomosyns may regulate DCV biogenesis. DCVs are formed at the trans-Golgi network (TGN) in a sequence of membrane fusion/ fission events ensuring correct packaging and processing of DCV cargos. Interestingly, tomosyn is enriched at the TGN (Figure 5 supplement 1) and the TGN area is reduced by 15% in DKO neurons, as shown by immunostaining of the TGN marker TMEM87A (Figure 5A-B). We therefore tested whether tomosyn regulates packaging and export of a neuropeptide cargo from the TGN using a modification of the Retention Using Selective Hooks (RUSH) method (Boncompain *et al*, 2012). In this method, streptavidin-binding peptide (SBP)-tagged secretory cargo is retained in the endoplasmic reticulum (ER) until addition of biotin due to the expression of the ER-localized streptavidin. Biotin disrupts SBP/streptavidin interaction and induces a synchronized transport of the cargo from the ER along the secretory pathway (Figure 5C-D). As a neuropeptide cargo, we used NPY fused to SBP and EGFP, as described previously (Emperador-Melero *et al*, 2018). In the absence of biotin, NPY-EGFP-SBP was diffusely distributed along cell soma and processes, in agreement with its localization to the ER. Addition of biotin induced a wave of NPY-EGFP-SBP accumulating in the Golgi first, and then leaving the Golgi as discrete puncta (Figure 5E, Figure 5 video 1). These puncta co-localized with an endogenous DCV marker, CHGA, indicating correct packaging of the NPY fusion protein into DCVs during the RUSH assay (Figure 5 supplement 2). Formation of such puncta and clearance of NPY-EGFP-SBP from the Golgi was observed in neurons of both genotypes. We next compared the speed of NPY-EGFP-SBP flux through the Golgi by plotting EGFP intensity within the Golgi area over time (Figure 5F). The peak of fluorescence intensity in the Golgi was reached 5.6 min faster in DKO than in WT, indicating that the speed of Golgi filling is increased in DKO (Figure 5G). The speed of Golgi clearance – determined by fitting a first order exponential decay curve to the data after the peak – was also increased (by 20%) in DKO neurons (Figure 5H). Thus, loss of tomosyns does not impede export of the overexpressed neuropeptide cargo from Golgi but, conversely, accelerates it.

We also traced the fate of newly made RUSH vesicles 90 minutes after addition of biotin. After the exit from Golgi, these vesicles travelled predominantly in one neurite, morphologically identified as the axon (Figure 5I). Most axonal vesicles (67%) traveled in the anterograde direction with a similar speed in neurons of both genotypes (Figure 5J-K), indicating that transport of newly made DCVs is not affected by the loss of tomosyns.

209 Since the increased rate of NPY trafficking through the Golgi does not explain the reduced levels
210 of DCVs and specific DCV cargos in DKO, we next tested if a more upstream process in DCV
211 production, i.e. expression of DCV genes, is impaired in the absence of tomosyns. To this end,
212 we tested mRNA expression of *Bdnf* (Figure 6A-B), some general DCV markers (Figure 6C), and
213 neuropeptides most abundantly expressed in hippocampal neurons (Figure 6D). Transcription
214 of the *Bdnf* gene yields at least nine transcripts, five of which were readily detectable in
215 cultured hippocampal neurons (Figure 6A). Of those, four were decreased in DKO neurons
216 (Figure 6B). The reduction in expression varied between transcript isoforms. DKO neurons
217 showed the strongest decrease (by 60%) in the isoform 1 mRNA, while levels of the isoform 6 –
218 a much less abundant transcript – were unaffected in DKO. All isoforms encode the same
219 protein, therefore reduced mRNA levels of the two highest expressed isoforms (1 and 4) can
220 explain markedly decreased BDNF levels in DKO neurons.

221 mRNA expression of all tested general DCV cargos was decreased in DKO as well (Figure 6C), in
222 close agreement with the changes observed in the proteomic analyses (Figure 3). Among
223 neuropeptide genes, *Grp* (gastrin related peptide) and *Pnoc* (nociceptin, nocistatin) showed the
224 strongest reduction in DKO (by 50% and 35%, respectively), while genes encoding
225 cholecystokinin, NPY, tachykinins and cortistatin displayed a reduction by around 30% (Figure
226 6D). Interestingly, somatostatin (*Sst*), a neuropeptide closely related to cortistatin, was
227 unaltered at the mRNA level in DKO neurons, indicating a certain specificity in expression
228 changes induced by the loss of tomosyns. Based on the single-cell transcriptomics data
229 (Saunders *et al*, 2018), expression of the affected genes was not confined to a specific neuronal
230 population (e. g. glutamatergic or GABAergic neurons). These data suggest that the loss of
231 tomosyns causes a widespread dysregulation in expression of general DCV cargos and specific
232 neuropeptides across different subpopulations of hippocampal neurons.

233 Since BDNF regulates expression of many secretory genes, including its own gene, we tested
234 whether the decreased mRNA levels of *Bdnf* and its known targets (*Vgf*, *Npy*) is a consequence
235 of a potentially decreased BDNF secretion (Figure 6E). We analyzed expression of *Bdnf*, Vgf and
236 *Npy* after treatment of neurons with recombinant BDNF (50 ng/ml for 3 h). Though this
237 treatment increased mRNA levels of *Bdnf* (isoform 1) and *Vgf* in neurons of both genotypes, it
238 did not rescue the impaired expression of these genes in DKO neurons (Figure 6F). *Npy*
239 expression did not respond to the BDNF treatment. Thus, decreased BDNF levels are not the
240 cause of the impaired DCV gene expression in the absence of tomosyns.

241 Transcription factor CREB is one of the few established regulators of neuronal DCV gene
242 expression in response to many factors, including BDNF and neuronal activity (Moore *et al*,
243 1996; Finkbeiner *et al*, 1997; Tao *et al*, 1998). We next tested whether overexpression of a
244 constitutively active form of CREB – carrying the Y134F mutation that lowers the threshold for
245 the activating S133 phosphorylation (Du *et al*, 2000) – rescues the transcriptional defect of DKO
246 neurons. This intervention failed to rescue expression of *Bdnf* and *Vgf* in DKO neurons (Figure
247 6G-H). In addition, levels of activated CREB (phosphorylated on S133) were not affected in DKO
248 neurons as evidenced by WB on neuronal lysates using a phospho-specific antibody (Figure 6
249 supplement 1). These data suggest that altered CREB activity does not account for the reduced
250 expression of *Bdnf* and other DCV cargo genes in DKO neurons.

251

Discussion

In this study, we examined the role of tomosyns in exocytosis of neuropeptide containing DCVs in mammalian neurons. Using pHluorin-based DCV fusion reporter, we found that the loss of tomosyns does not alter DCV exocytosis but lowers intracellular levels of the DCV reporter. We corroborated the latter finding by showing that levels of many endogenous DCV cargos are decreased in tomosyn DKO neurons by three independent approaches (ICC, WB, and mass spectrometry). The effect on DCV pool and/or composition was accompanied by a smaller DCV size, increased speed of the DCV reporter flux through the TGN, and decreased mRNA levels of many (but not all) DCV cargos. Taken together, these data suggest that tomosyn is dispensable for the control of DCV fusion, but, paradoxically, has an impact on the expression of DCV genes and intracellular neuropeptide levels.

The lack of the effect on neuronal DCV fusion is surprising, given that tomosyn regulates SV release in neurons and secretory granule exocytosis in neuroendocrine cells and platelets. However, phenotypes caused by the loss of tomosyn expression in different cell types are discrepant. While loss of tomosyn resulted in enhanced SV fusion in the mouse brain and invertebrate nervous system (Sakisaka *et al*, 2008; Ben-Simon *et al*, 2015; Gracheva *et al*, 2006; McEwen *et al*, 2006; Chen *et al*, 2011; Sauvola *et al*, 2021), tomosyn deficiency in platelets, INS-1E cells and rat superior cervical ganglion neurons led to an opposite phenotype – a strong reduction in secretion (Ye *et al*, 2014; Zhu *et al*, 2014; Cheviet *et al*, 2006; Baba *et al*, 2005). No unifying model explains the discrepant effects of tomosyn on vesicle fusion.

DCVs and SVs differ in release properties, and recent studies shed light on some components of the molecular machinery contributing to these differences (Persoon *et al*, 2019; Moro *et al*, 2021). In contrast to SVs, which are released in response to a single electric pulse, neuronal DCVs require prolonged high-frequency stimulation for induction of exocytosis (Hartmann *et al*, 2001; Xia *et al*, 2009; Persoon *et al*, 2018). Several factors can explain the reluctance of DCV to fuse, among them the loose coupling of DCVs to the sites of calcium entry, requiring an increase in calcium levels reaching beyond an immediate radius of a calcium channel (Mansvelder & Kits, 2000). Interestingly, the inhibitory effect of tomosyn on DCV fusion in adrenal chromaffin cells is calcium-dependent and could be overridden by an increase in intracellular calcium (Yizhar *et al*, 2004). Thus, it is possible that under high-frequency stimulation required for the induction of neuronal DCV exocytosis, the regulatory effect of tomosyn on vesicle fusion is lost.

Altogether, the discrepant effects of tomosyn on fusion in different cell types suggest that tomosyn does not act solely as an inhibitor of fusogenic SNARE complex formation. In line with this, loss of tomosyns in primary neurons did not alter the amount of assembled ternary SDS-resistant SNARE complexes (Figure 1H). In addition to the SNARE domain, tomosyn contains multiple WD40-repeats folded into two bulky beta-propellers. The two propellers are, in fact, the largest and evolutionary best conserved part of tomosyn. Several interaction partners of tomosyn, such as synapsin and Rab3, bind to the propeller domain (Cazares *et al*, 2016). These interactions may mediate targeting of tomosyn to SV membrane (Takamori *et al*, 2006) and act in tomosyn-dependent regulation of SV pools (Cazares *et al*, 2016). Interestingly, yeast orthologs of tomosyn, SRO7 and SRO77, localize to post-Golgi vesicles and act as vesicle tethers at the plasma membrane via interaction with the RAB3 ortholog Sec4 GTPase (Lehman *et al*,

1999; Rossi *et al*, 2018). Thus, tomosyn may affect steps far upstream of vesicle fusion via WD40-domain mediated interactions. In this case, the effect of tomosyn on exocytosis of different types of vesicles would depend on the mechanisms of vesicle tethering/ docking, which differ between SVs and DCVs. Tomosyn co-purifies with DCVs in chromaffin cells (Wegrzyn *et al*, 2010) and travels together with DCVs in neurons (Geerts *et al*, 2017) but its loss did not affect neuronal DCV distribution and trafficking (Figure 2A-D, 5J-K), suggesting that tomosyn is dispensable for DCV tethering in neurons.

Despite the lack of effect on DCV exocytosis, loss of tomosyns resulted in reduced intracellular levels of many DCV cargos. The latter phenotype is consistent with the effect of tomosyn in platelets, where its loss led to a strong decrease in many secretory cargos, despite the fact that the release of these cargos was reduced, not enhanced (Ye *et al*, 2014). Similarly, loss of SRO7/77 in yeast resulted in the accumulation of secretory vesicles with an altered composition (Forsmark *et al*, 2011). Taken together, these data suggest a role of tomosyn and its orthologs in the formation of secretory granules. The accumulation of tomosyn at the TGN (Figure 5 supplement 1) and decreased DCV size in DKO neurons (Figure 4A-C) are consistent with such a role. However, loss of tomosyns did not impair formation of new NPY vesicles in the RUSH assay, indicating that tomosyns are dispensable for DCV biogenesis (Figure 5E, Figure 5 video 1). Interestingly, NPY flux through the Golgi was slightly accelerated in the absence of tomosyns (Figure 5F-H), which, in combination with the decreased TGN size in DKO, suggests a role of tomosyn(s) in the TGN membrane trafficking. Knockdown of tomosyn in hippocampal neurons was shown to modulate activity of RhoA GTPase (Shen *et al*, 2020), which, in turn, regulates membrane trafficking at the Golgi (Quassollo *et al*, 2015). On the other hand, the decreased TGN size can be explained by the reduced expression of many secretory cargos in DKO neurons, since Golgi size is regulated by the secretory cargo load (Sengupta & Linstedt, 2011).

The most unexpected observation of this study is a decrease in mRNA expression of many DCV cargos in DKO neurons (Figure 6B-D), suggesting a role of tomosyn(s) in regulation of the DCV gene transcription. We ruled out the simplest mechanism of such regulation, whereby decreased BDNF levels in DKO would result in an impaired transcriptional feedback loop. Treatment of DKO neurons with BDNF, as well as overexpression of the activated CREB that mediates this autoregulation (Esvald *et al*, 2020), did not rescue decreased *Bdnf* and *Vgf* mRNA levels (Figure 6F-H). Considering the established effect of tomosyn on SV exocytosis and synaptic activity, it is possible that altered neuronal firing patterns contribute to the decreased expression of DCV genes in DKO. *Bdnf* and many neuropeptide genes are known targets of activity-dependent signal transduction (Zafra *et al*, 1990; Ernfors *et al*, 1991; Isackson *et al*, 1991; MacArthur & Eiden, 1996). If indeed caused by chronically altered firing patterns, the transcriptional defect of DKO neurons is cell-autonomous, since the decrease in BDNF was detected in both single neuron and network cultures. In addition to the decreased mRNA expression of DCV genes, other factors likely contribute to the reduction of DCV cargos in DKO neurons, since loss of tomosyns also affected levels of the DCV fusion reporter expressed under control of the synapsin promoter, even after silencing of neuronal activity with TTX and despite the normal activity of this promoter in DKO (Figure 1H-I, Figure 1 supplement 3).

In summary, our current findings indicate that tomosyns are dispensable for neuronal DCV exocytosis but regulate intracellular neuropeptide levels. Decreased levels of many

337 neuropeptides and BDNF at the critical moment of neuronal development may promote the
338 onset of neurodevelopmental disorders associated with mutations in *STXBP5/5L* genes.

339

Materials and methods

Mice

Stxbp5$^{lox/lox}$, *Stxbp5l*$^{lox/lox}$ double conditional null mice were generated by breeding two lines with the individually targeted *Stxbp5* and *Stxbp5l* alleles. To generate *Stxbp5*$^{lox/+}$ mice, *lox2272* recombination sites flanking exon 2 of *Stxbp5* (98 bp in size) were introduced into the genome via homologous recombination in C57Bl/6 embryonic stem (ES) cells (Cyagen Animal Model Services, Santa Clara, USA). Lox2272 recombines efficiently with other lox2272 sites, but not with loxP (Lee & Saito, 1998). Deletion of exon 2 causes a frameshift in all tomosyn reference transcripts (NM_001081344.3, NM_001408063.1, NM_001408064.1 and NM_001408065.1). The targeting vector contained a neomycin resistance marker, flanked by self-deleting anchor sites and placed between exon 2 and the lox2272 site in intron 2. Targeted ES clones were injected into blastocysts to produce germ-line chimeras, which were mated to C57Bl/6J wild-type mice. *Stxbp5* line genotyping was performed using the following primers (5' ACTTAGCGCGGAGGGTTTTGTC 3' and 5' CGTAGGCTTTTAAATCACCGCTGT 3') to amplify *Stxbp5*$^{+}$ or S*txbp5*^{lox} specific products of 196 and 236 bp in size, respectively.
The *Stxbp5l*$^{lox/+}$ line was generated independently as described in (Geerts *et al*, 2015). In these mice, the paralogous exon 3 (also 98 bp in size) is flanked by loxP sites. Cre-mediated excision induces a frameshift in all reference transcripts (NM_172440.3, NM_001114611.1, NM_001114612.1, NM_001114613.1, also named xb-, s-, b- and m-tomosyn-2, respectively). *Stxbp5l* line genotyping was performed for *Stxbp5l* as described (Geerts *et al*, 2015).
After interbreeding the two mouse lines, both backcrossed to an inbred C57Bl/6J genetic background, newborn pups from homozygous *Stxbp5*$^{lox/lox}$, *Stxbp5l*$^{lox/lox}$ matings were used for the preparation of neuronal cultures in all the described experiments. Mice were housed and used for experiments according to institutional guidelines and Dutch laws.

Neuronal cultures

Mouse hippocampal cultures were prepared from newborn pups. Normally, hippocampi from several pups from one nest were pooled in one culture preparation, which was considered as one biological replicate. Hippocampi were dissected in Hanks Balanced Salt Solution (HBSS, Sigma H9394) supplemented with 10 mM HEPES (pH 7.2-7.5, Gibco™ 15630056) and digested with 0.25% trypsin (Gibco™ 15090046) at 37°C for 15 min. After the digestion, tissue pieces were washed in HBSS and triturated using fire-polished Pasteur pipettes in Dulbecco's modified Eagle medium (DMEM, VWR Life Science VWRC392-0415) supplemented with 10% fetal calf serum (FCS, Gibco™ 10270), non-essential amino acids (Sigma M7145), and antibiotics (penicillin/ streptomycin, Gibco™ 15140122). For most immunocytochemistry (ICC) experiments, cell suspension was sparsely plated on a feeder layer of rat glia at a density of 20-30*10^3/ well on 15 mm coverslips. For BDNF ICC and pHluorin imaging experiments, neurons were plated on glial micro-islands at a density of 1500/ well (to obtain single neuron cultures). For RUSH, rat glia were omitted, and neurons were plated on glass coverslips at a density of approximately 120*10^3/ well on 15 mm coverslips. Prior to plating, glass coverslips were coated with poly-L-ornithine (Sigma P4957) and laminin (Sigma L2020). For western blot, proteomics, electron microscopy and qPCR experiments, neurons were plated on coated plastic without the glia feeder layer at a density of 400*10^3/ well in a 6-well plate. Cultures were maintained in a

383 humified incubator at 37 °C and 5% CO_2 in Neurobasal medium (Gibco™ 21103049)
384 supplemented with B27 (Gibco™ 17504044), 10 mM HEPES, GlutaMAX™ (Gibco™ 35050038)
385 and antibiotics (penicillin/ streptomycin, Gibco™ 15140122). To induce loss of tomosyns,
386 cultures were transduced within 8 h after plating with a lentivirus encoding Cre-recombinase
387 expressed under control of synapsin promoter (pSyn-Cre-mCherry). As control, neurons from
388 the same culture preparation were transduced with *Cre*-recombinase lacking the DNA-binding
389 domain (pSyn-ΔCre-mCherry). Experiments were performed, if not otherwise stated, on day *in*
390 *vitro* (DIV) 14.
391 Rat glia were prepared from cortices of newborn rats. Cortices were digested in papain
392 (Worthington Biochemical Corporation LS003127) at 37°C for 45 min and triturated in DMEM
393 supplemented with 10% FCS, non-essential amino acids, and antibiotics. Glia were plated and
394 expanded in T175 flasks. For making single neuron cultures, glia were plated on micro-islands of
395 growth permissive substrate (mix of collagen I and poly-D-lysine, Corning 354236 and Sigma
396 P6407, respectively) that were printed on a layer of 0.15% agarose.
397
398 **Expression constructs**
399 All transgenes, except for the RUSH reporter, were expressed under control of human synapsin
400 promoter in lentiviral backbones. Cre-mCherry and ΔCre-mCherry fusions were described in
401 (Wolzak *et al*, 2022). Generation of the DCV fusion reporter (pre-NPY-pHluorin) was described
402 in (Nassal *et al*, 2022). Construct encoding constitutively active CREB mutant (Y134F) was
403 described in (Moro *et al*, 2020). RUSH reporter (Streptavidin-KDEL-IRES-SBP-EGFP-NPY) was
404 expressed under control of the CMV promoter in pIRESneo3 backbone. Generation of this
405 reporter was described in (Emperador-Melero *et al*, 2018).
406
407 **Visualization and analysis of DCV fusion**
408 Single neuron cultures were transduced on DIV8 with a lentivirus encoding the N-terminal part
409 of human NPY fused to super-ecliptic pHluorin (Figure 1 supplement 2). DIV14-15 neurons were
410 used for live imaging on a Nikon Ti Eclipse inverted microscope equipped with A1R confocal
411 module and Andor DU-897 camera (with 512x512 pixels frame) under 40x oil objective
412 (numerical aperture, NA 1.3). LU4A laser unit with 488 nm wavelength laser was used as the
413 illumination source. Coverslips were transferred in an imaging chamber in Tyrode's solution
414 (119 mM NaCl, 2.5 mM KCl, 2 mM $CaCl_2$, 2 mM $MgCl_2$, 25 mM HEPES and 30 mM Glucose, pH
415 7.4, 280 mOsmol) and time-lapse videos were recorded at 2 Hz frequency for 2 min at room
416 temperature under constant perfusion with Tyrode's. After 30 sec of baseline recording,
417 neurons were subjected to electric field stimulation (16 trains, each consisting of 50 pulses at
418 50 Hz and separated by 500 msec intervals) delivered by platinum electrodes. At the end of
419 each recording, 50 mM NH_4Cl-containing Tyrode's solution (with NaCl concentration reduced to
420 69 mM to maintain osmolarity) was applied to visualize the intracellular pool of DCVs.
421 Analysis of the time-lapse recordings was performed as described (Persoon *et al*, 2019). In
422 short, fusion events were detected by a sudden rise in fluorescence intensity. 3x3 pixel regions
423 of interest (ROI) were placed on time-lapse recordings using a custom-made script in Fiji
424 (Schindelin *et al*, 2012). Change in fluorescence intensity (F) within these ROIs was plotted as
425 $\Delta F/F_0$, where F_0 is an average of the first 10 frames of acquisition. Resulting traces were checked
426 using a custom-made script in MATLAB, and only events with $F/F_0 \geq 2$ SD and rise time < 1 sec

were counted. Total number of intracellular vesicles (intracellular pool) was determined as the number of fluorescent puncta after the ammonium pulse corrected to account for overlapping puncta. Released fraction was calculated as the number of fusion events per neuron divided by the intracellular pool of DCVs.

Immunocytochemistry

Neurons grown on coverslips were fixed by application of phosphate-buffered saline (PBS) containing 4% paraformaldehyde (PFA, Sigma P6148) and 4% sucrose for 10 min. After fixation, neurons were washed and the residual PFA was quenched by application of 0.1 M glycine for 5 min. Neurons were permeabilized and blocked in PBS containing 0.1% Triton™ X-100 (Fisher Chemical T/3751/08) and 2% normal goat serum (Gibco™ 16210-072) ('blocking buffer') for 30 min. Primary antibodies diluted in blocking buffer were applied for 1 h at room temperature. Primary antibodies used in this study and their dilutions are listed in Table 1. After washing with PBS, neurons were incubated with Alexa Fluor-coupled secondary antibodies diluted at 1:500 for 45 min. Stained coverslips were mounted in Mowiol.

Confocal microscopy of fixed neurons

Imaging of stained neurons was performed on a Nikon Ti Eclipse inverted microscope equipped with A1R confocal module and LU4A laser unit. Images were acquired under 40x (NA 1.3) or 60x (NA 1.4) oil objectives in the confocal mode. Acquisition parameters (zoom, image size, scanning speed, laser power and gain) were set using NIS software to achieve appropriate image resolution and avoid signal saturation. Three to five z-sections with an interval of 0.2 µm were collected per image.

Analysis of staining intensity was performed on maximum intensity projection of z-stacks using a custom-made macro in Fiji, as described (Moro *et al*, 2020). Masks of the neuronal somata and neurites were obtained based on MAP2 signal. Puncta of DCV cargos (BDNF, IA-2) were detected within the neurite mask based on their intensity and dimensions.

SDS-PAGE western blot (WB) analysis

To analyze protein levels, high-density neuronal cultures ($400*10^3$/well in a 6-well plate) were lysed in Laemmli sample buffer. Lysates were heated at 95℃for 5 min, separated by SDS-PAGE using either home-made tris-glycine or commercially available Mini-PROTEAN TGX Stain-Free gels (Bio-Rad 4568096), and transferred to nitrocellulose membrane (Bio-Rad 1620115) using wet tank transfer method. Membranes were blocked in 5% milk powder dissolved in Tris-buffered saline containing 0.1% Tween® 20 (TBS-T). Membranes were incubated with primary antibodies diluted in TBS-T on a shaking platform overnight at 4℃. Primary antibodies used in this study and their dilutions are listed in Table 1. Horseradish peroxidase coupled secondary antibodies were applied at 1:10000 dilution for 1 h at room temperature. Chemiluminescence-based detection was performed using SuperSignal West Femto Maximum Sensitivity Substrate (Thermo Scientific 34095) on the Odissey Fc imaging system (LI-COR Bioscience). Signal intensities of bands of interest were analyzed using Image Studio Lite Software and normalized to the intensity of a loading control (actin or tubulin). Actin levels were not affected by the loss of tomosyn, as evidenced by comparing band intensities of actin to total protein stain visualized on Mini-PROTEAN TGX Stain-Free gels.

471

472 **Table 1.** List of primary antibodies used in this study.

Antigen	Catalogue number	Type of experiment	Dilution
Syntaxin 1	Sigma S0664	WB	1:2000
Tomosyn	Synaptic Systems 183103	WB	1:1000
		ICC	1:500
Tomosyn-2	Synaptic Systems 183203	WB	1:1000
alpha-Tubulin	Synaptic Systems 302211	WB	1:1000
Actin	Merck MAB1501	WB	1:1000
Synaptophysin	Synaptic Systems 101004	ICC	1:1000
MAP2	Abcam ab5392	ICC	1:5000
IA-2 (PTPRN)	Merck MABS469	ICC, WB	1:100
CHGA	Synaptic Systems 259003	ICC	1:500
CHGB	Synaptic Systems 259103	ICC	1:500
BDNF	DSHB hybridoma product BDNF #9 (supernatant) *	ICC	1:4
LAMP1	DSHB hybridoma product 1D4B (supernatant) **	ICC	1:20
		WB	1:200
LIMP2	Novus Biologicals NB400-129	WB	1:1000
TMEM87A	Novus Biologicals NBP1-90532	ICC	1:100
TGN38	Bio-Rad AHP499G	ICC	1:100
pCREB (S133)	R&D Systems MAB6906	ICC	1:50
		WB	1:1000

473 * This monoclonal antibody developed by Barde Y.-A. was obtained from the Developmental
474 Studies Hybridoma Bank, created by the NICHD of the NIH and maintained at The University of
475 Iowa, Department of Biology, Iowa City, IA 52242.
476 ** This monoclonal antibody developed by August J.T. was obtained from the Developmental
477 Studies Hybridoma Bank, created by the NICHD of the NIH and maintained at The University of
478 Iowa, Department of Biology, Iowa City, IA 52242.
479

480 **Detection of SNARE complexes**

481 Detection of SNARE complexes was performed as described previously (Hayashi *et al*, 1994;
482 Otto *et al*, 1997). The protocol is based on the observation that assembled synaptic SNARE
483 complexes (consisting of syntaxin-1, SNAP25 and VAMP2) are preserved in SDS-containing lysis
484 buffer ('SDS-resistant') but sensitive to temperatures higher than 60℃. To detect syntaxin-1 in
485 SNARE complexes, high-density neuronal cultures (400K/well in a 6-well plate) were lysed in 1%
486 SDS-containing Laemmli sample buffer, passed through insulin syringe and split in two parts.
487 The first part of the lysates was heated at 95℃ for 5 min (for the detection of total syntaxin-1),
488 while the second part was heated at 37℃ for 5 min (for the detection of syntaxin-1 in SNARE
489 complexes). Lysates were separated by SDS-PAGE using 4-20% gradient gels (Mini-PROTEAN
490 TGX Stain-Free gels, Biorad #4568096). Protein transfer and detection were performed as
491 described above.

492

493 **Proteome analysis by mass spectrometry**

494 DIV12-13 hippocampal neurons grown in high density cultures (400*10^3/ well in a 6-well plate)
495 were washed once with pre-warmed PBS and lysed in Laemmli sample buffer (50 µl/ well).
496 Lysates were passed through insulin syringe and stored at -80°C until further processing.
497 In-gel digestion with Trypsin/Lys-C Mix solution (Promega) was performed as previously
498 described (Gonzalez-Lozano & Koopmans, 2019). Peptides were analyzed by micro LC-MS/MS
499 using a TripleTOF 5600 mass spectrometer (Sciex, Framingham, MA, USA). The peptides were
500 fractionated with a linear gradient of acetonitrile using a 200 mm Alltima C18 column (300 µm
501 i.d., 3 µm particle size) on an Ultimate 3000 LC system (Dionex, Thermo Scientific, Waltham, MA,
502 USA). Data-independent acquisition was used with Sequential Window Acquisition of all
503 THeoretical mass spectra (SWATH) windows of 8 Da, as previously described (Gonzalez-Lozano
504 *et al*, 2021).
505 SWATH data was analyzed using DIA-NN (v1.8) (Demichev *et al*, 2020). A spectral library was
506 generated from the complete mouse proteome with a precursor m/z range 430-790. Data was
507 searched with 20 ppm mass accuracy, match-between-runs algorithm (MBR) enabled and robust
508 LC as quantification strategy. Propionamide was selected as fixed modification. Downstream
509 analysis was performed using MS-DAP (v1.0, https://github.com/ftwkoopmans/msdap)
510 (Koopmans *et al*, 2022). The experimental replicate with the lowest number of identified
511 peptides was removed from the analysis (for both genotypes). Only peptides identified and
512 quantified in at least four out of five remaining replicates per genotype were included in the
513 analysis. Normalization was achieved using variance stabilization normalization (Vsn) and mode-
514 between protein methods. The Msqrob algorithm was selected for differential expression
515 analysis, using an FDR adjusted p-value threshold of 0.01 and log2 fold change of 0.3 to
516 discriminate significantly regulated proteins. All data are available in PRIDE repository with the
517 identifier PXD038442. Gene ontology enrichment analysis of the differentially expressed proteins
518 was performed using ShinyGO application v0.75 with an FDR adjusted p-value threshold of 0.05
519 (http://bioinformatics.sdstate.edu/go/) (Ge *et al*, 2020).

520

521 **Electron microscopy**

522 Neurons grown on coated glass coverslips were fixed on DIV14 in 2.5% glutaraldehyde in 0.1M
523 cacodylate buffer. The cells were postfixed in 1% osmium/1% ruthenium and subsequently
524 dehydrated by increasing ethanol concentrations (30%, 50%, 70%, 90%, 96% and 100%) before
525 embedding in EPON. After polymerization of the resin for 72 h at 65 °C, glass coverslips were
526 removed by heating the samples in boiling water. Neuron-rich regions were selected by light
527 microscopy, cut out and mounted on pre-polymerized EPON cylinders. Ultrathin sections of 70-
528 90 nm were cut on an ultra-microtome (Reichert-Jung, Ultracut E) and collected on formvar-
529 coated single slot grids. Finally, the sections were contrasted with uranyl acetate and lead
530 citrate in an ultra-stainer (Leica EM AC20) and imaged in a JEOL1010 transmission electron
531 microscope (JEOL) at 60 kV while being blinded for the experimental conditions. Synapses,
532 somas and DCV-rich areas were photographed by a side-mounted Modera camera (EMSIS
533 GmbH). While remaining blinded for experimental conditions, DCV diameters were measured in

534 iTEM software (Olympus) and synapse parameters were quantified in a custom-written
535 software running in Matlab (Mathworks).
536
537 **RUSH assay**
538 The protocol is modified from (Boncompain *et al*, 2012). Neurons were grown in standard
539 neuronal medium except Neurobasal without phenol red (Gibco™ 12348017) was used to
540 minimize an autofluorescent background during live imaging. On DIV7, half of the medium was
541 refreshed with the same medium lacking B27 supplement (to reduce extracellular biotin levels).
542 On DIV9, neurons were transfected using the calcium phosphate transfection method with a
543 plasmid encoding a DCV reporter and an ER hook (pCMV-Streptavidin-KDEL-IRES-SBP-EGFP-
544 NPY) together with a 'filler' plasmid (pCMV-mCherry). Neurons were imaged live approximately
545 16h after the transfection upon addition of 40 µM biotin to the conditioned medium. Time-
546 lapse imaging was performed on a Nikon Ti Eclipse inverted microscope equipped with A1R
547 confocal module under 40x oil objective (NA 1.3). LU4A laser unit with 488 nm wavelength laser
548 was used as the illumination source. Neurons were picked for imaging based on the mCherry
549 fluorescence and were imaged at 37°C and 5% CO_2 for 2 h after addition of biotin, at a
550 frequency of 1 frame/ 5 min.
551 Movies were analyzed in Fiji. Possible lateral drift during recordings was corrected using the
552 Image Stabilizer plugin. Mean intensity of NPY-EGFP within the Golgi mask was measured
553 across the frames and plotted against time in GraphPad Prism. The rate constant of Golgi
554 clearance was determined by fitting a one phase exponential decay curve to the decay phase of
555 the intensity plot.
556 For imaging of DCV trafficking in neurites, transfected neurons were imaged in 80 min after
557 addition of biotin with 0.5 Hz frequency (3 min recordings). Kymographs (space/time plots)
558 were generated from time-lapse videos in Fiji using the KymoResliceWide plugin. Kymographs
559 were analyzed using Kymobutler software (Jakobs *et al*, 2019).
560
561 **Quantitative RT-PCR (qRT-PCR)**
562 RNA extraction from neuronal cultures was performed using ISOLATE II RNA Micro Kit (Meridian
563 Bioscience BIO-52073). cDNA was synthesized from purified RNA using SensiFast cDNA
564 Synthesis Kit (Meridian Bioscience BIO-65054). qRT-PCRs were run on a QuantStudio 5 system
565 (ThermoFisher Scientific) using SensiFast SYBR Lo-ROX Kit (Meridian Bioscience BIO-94020).
566 qRT-PCR primers (listed in Table 2) were validated for the efficiency by running qRT-PCRs on 10-
567 fold serial dilutions of cDNA, and for the specificity estimated from melt curves. Only primers
568 with an efficiency of 90-105% were used for experiments. Fold changes (FC) in gene expression
569 were determined using the cycle threshold (CT) comparative method (2^{-ddCT}) using *Gapdh* as a
570 housekeeping gene. *Gapdh* CT values were not affected by the genotype or treatment applied.
571 Statistical analysis of the data was performed on log-transformed data (logFC, ddCT).
572
573 **Table 2.** List of qRT-PCR primers used in this study

Gene	Forward primer sequence	Reverse primer sequence
Bdnf (transcript 1)	ACTGAGCAAAGCCGAACTT	TCTCACCTGGTGGAACATTGTG
Bdnf (transcript 2)	TAGGCTGGAATAGACTCTTGG	CTCACCTGGTGGAACTTCTTTG

Bdnf (transcript 4)	CCTCCCCCTTTTAACTGAAG	CTCACCTGGTGGAACTTTTT
Bdnf (transcript 6)	AGGGACCAGAAGCGTGACAA	CTCACCTGGTGGAACTCAGGGT
Bdnf (transcript 9)	TGATTGTGTTTCTGGTGACA	CGGTTTCTAAGCAAGTGAAC
Vgf	CTTTGACACCCTTATCCAAGGCG	GCTAATCCTTGCTGAAGCAGGC
Pcsk1	GGAGAGAATCCTGTAGGCACCT	GCTCTGGTTGAGAAGATGTCCC
Pam	AGTCGGATCGTGCAGTTCTCAC	ACTGGTTCAGGTGAGGCACAAG
Ptprn	TGGCAGGCTATGGAGTAGAGCT	CTTGACATCGGCTCCTCCAACA
Scg2	CAGGAAGAGGTGAGAGACAGCA	TGGAGGCATCCTCTGAGAGTTG
Npy	TACTCCGCTCTGCGACACTACA	GGCGTTTTCTGTGCTTTCCTTCA
Cck	GAGGTGGAATGAGGAAACAA	CAGATTTCACATTGGGGACT
Grp	TTCAAACCGCTAAGTTGGT	GAAGGGTTTTGTTTTGCTCC
Sst	TCTGGAAGACATTCACATCC	TTCTAATGCAGGGTCAAGTT
Tac1	AGATCTCTCACAAAAGGCAT	CATCGCGCTTCTTTCATAAG
Pnoc	TCCTCTTTTGTGACGTTCTG	GAGGATGCACGTCTTTAAGT
Vip	ATGATGTGTCAAGAAATGCC	ATTCGTTTGCCAATGAGTGA
Pdyn	ATCAACCCCCTGATTTGCTC	ATCTTCCAAGTCATCCTTGC
Penk	ACATCAATTTCCTGGCGTGC	TGTTATCCCAAGGGAACTCG
Cort	CTTCTTATGTCAGCTTTGCC	CTCCAATCCCTTAGTTGACC
Gapdh	CATCACTGCCACCCAGAAGACTG	ATGCCAGTGAGCTTCCCGTTCAG

Statistical analyses

Sample size was chosen based on the previously published findings from similar experiments using similar measuring techniques. Statistical analyses were performed using GraphPad Prism software. Data distribution was tested for normality using the D'Agostino-Pearson test. Possible outliers were identified using the ROUT method. An F test was used to compare variances between the groups. Statistical tests were chosen based on the distribution of the data sets, as well as on the number of groups being compared. Statistical tests used in individual experiments are specified in the corresponding figure legends. Full statistical information, including exact p-values, is provided in Table 3.

Table 3. Summary of statistical analyses applied in this study

Figure	Dataset	Groups	n-number*	Statistical test	*p*-value
1B	Cumulative number of DCV fusion events per neuron plotted against time	WT DKO	3 (36) 3 (34)	Two-way repeated measures ANOVA	$p_{\text{time x genotype}} = 0.4823$ $p_{\text{time}} < 0.0001$ (****) $p_{\text{genotype}} = 0.3166$
1C	Total number of DCV fusion events / neuron	WT DKO	3 (36) 3 (34)	Mann-Whitney test	$p = 0.0970$
1D	Number of intracellular NPY-pHluorin puncta/ neuron	WT DKO	3 (36) 3 (35)	Unpaired t test	$p = 0.0224$ (*)
1E	Fraction of released DCVs (% total pool)	WT DKO	3 (36) 3 (34)	Two-way repeated measures ANOVA	$p_{\text{time x genotype}} > 0.9999$ $p_{\text{time}} < 0.0001$ (****)

					$p_{genotype}$ = 0.9014
1F	Fluorescence intensity peaks (averaged per neuron)	WT DKO	3 (36) 3 (34)	Mann-Whitney test	p = 0.4509
1G	Band intensities of syntaxin-1 complexes (WB)	DKO (% WT)	4 cultures	One sample t test (compare to 100%)	p_{37kDa} = 0.2858 $p_{80\ kDa}$ = 0.5714 $p_{200\ kDa}$ = 0.0002 (***)
1I	Intensity of NPY-pHluorin in network cultures (neurites)	WT DKO	3 (23) 3 (24)	Unpaired t test with Welch's correction	p < 0.0001 (****)
	Intensity of NPY-pHluorin in network cultures (soma)	WT DKO	3 (23) 3 (23)	Unpaired t test with Welch's correction	p = 0.0014 (**)
1 suppl 1E	Dendrite length/ neuron	WT DKO	3 (30) 3 (28)	Unpaired t test	p = 0.5902
1 suppl 1F	Number of synaptophysin puncta/ mm dendrite	WT DKO	3 (30) 3 (28)	Unpaired t test	p = 0.1380
1 suppl 1G	Intensity of synaptophysin signal in neurites	WT DKO	3 (30) 3 (28)	Unpaired t test	p = 0.6561
1 suppl 3B	Intensity of EGFP expressed under control of synapsin promoter (neurites)	WT DKO	3 (30) 3 (28)	Unpaired t test	p = 0.0867
	Intensity of EGFP expressed under control of synapsin promoter (soma)	WT DKO	3 (30) 3 (28)	Unpaired t test	p = 0.0541
1 suppl 3D	Intensity of EGFP expressed under SYN1 promoter (neurites)	WT DKO	3 (30) 3 (28)	Unpaired t test	p = 0.0898
	Intensity of EGFP expressed under SYN1 promoter (soma)	WT DKO	3 (30) 3 (28)	Unpaired t test	p = 0.0541
2B	Intensity of BDNF (neurites)	WT DKO	3 (32) 3 (35)	Mann-Whitney test	p < 0.0001 (****)
	Intensity of BDNF (soma)	WT DKO	3 (32) 3 (35)	Mann-Whitney test	p < 0.0001 (****)
2D	Intensity of IA-2 (neurites)	WT DKO	3 (24) 3 (24)	Unpaired t test	p < 0.0001 (****)
	Intensity of IA-2 (soma)	WT DKO	3 (24) 3 (24)	Unpaired t test	p = 0.0472 (*)
2E	Band intensities of IA-2 (WB)	DKO (% WT)	3 (9)	One sample t test (compare to 100%)	p < 0.0001 (****)
2 suppl 1B	Intensity of LAMP1	WT DKO	2 (10)	Unpaired t test	p = 0.9847

2 suppl 1D	Band intensities of LAMP1 (WB)	DKO (% WT)	3 (9)	One sample t test (compare to 100%)	p = 0.3716
	Band intensities of LIMP2 (WB)	DKO (% WT)	3 (9)	One sample t test (compare to 100%)	p = 0.7225
4B	DCV diameter	WT DKO	3 (135 DCVs) 3 (64 DCVs)	Unpaired t test on means from three independent cultures	p = 0.0129 (*)
4E	SV diameter	WT DKO	3 (621 SVs) 3 (617 SVs)	Unpaired t test on means from three independent cultures	p = 0.2234
4F	Number of SV/ synapse	WT DKO	3 (149 synapses) 3 (147 synapses)	Unpaired t test on means from three independent cultures	p = 0.4713
4G	Length of active zone	WT DKO	3 (151 synapses) 3 (148 synapses)	Unpaired t test on means from three independent cultures	p = 0.4366
4H	Length of PSD	WT DKO	3 (152 synapses) 3 (147 synapses)	Unpaired t test on means from three independent cultures	p = 0.3752
5B	TGN area	WT DKO	3 (40) 3 (39)	Unpaired t test	p = 0.0001 (***)
	Nucleus area	WT DKO	3 (40) 3 (39)	Unpaired t test	p = 0.1847
5F	NPY-EGFP intensity in the Golgi plotted against time	WT DKO	3 (33) 3 (30)	Two-way repeated measures ANOVA	$p_{\text{time x genotype}}$ = 0.0014 (**) p_{time} < 0.0001 (****) p_{genotype} = 0.3280
5G	Time required to reach maximum NPY-EGFP intensity in the Golgi	WT DKO	3 (34) 3 (28)	Unpaired t test	p = 0.0444 (*)
5H	Rate constants of NPY-EGFP export from the Golgi	WT DKO	3 (34) 3 (30)	Unpaired t test	p = 0.0276 (*)
5J	% anterograde DCVs	WT DKO	2 (12) 2 (12)	Unpaired t test	p = 0.9488
	% retrograde DCVs	WT DKO	2 (12) 2 (12)	Unpaired t test	p = 0.7938
5K	Speed of anterogradely trafficking DCVs	WT DKO	2 (11) 2 (12)	Unpaired t test	p = 0.8107
6B	mRNA expression of *Bdnf* transcript isoforms	DKO (logFC relative to WT)	8 cultures	One sample t test (compare to $\log_2$FC=0)	p_{tr1} = 0.0003 (***) p_{tr2} = 0.0032 (**) p_{tr4} < 0.0001 (****) p_{tr6} = 0.1183 p_{tr9} = 0.0012 (**)
6C	mRNA expression of general DCV cargos	DKO (logFC	8 cultures	One sample t test (compare to $\log_2$FC=0)	p_{Vgf} = 0.0006 (***) p_{Pcsk1} = 0.0006 (***) p_{Pam} = 0.0032 (**)

		relative to WT)			p_{Ptprn} = 0.0187 (*) p_{Scg2} = 0.0177 (*)
6D	mRNA expression of general DCV cargos	DKO (logFC relative to WT)	8 cultures	One sample t test (compare to $log_2FC=0$)	p_{Npy} = 0.0002 (***) p_{Cck} = 0.0016 (**) p_{Grp} = 0.0003 (***) p_{Sst} = 0.6986 p_{Tac1} = 0.0201 (*) p_{Pnoc} = 0.0023 (**) p_{Vip} = 0.7972 p_{Pdyn} = 0.8905 p_{Penk} = 0.4408 p_{Cort} = 0.0267 (*)
6F	mRNA expression of *Bdnf* (transcript isoform 1) upon BDNF treatment	WT ± BDNF DKO ± BDNF	4 cultures	Two-way repeated measures ANOVA	$p_{treatment\ X\ genotype}$ = 0.1225 $p_{treatment}$ = 0.0190 (*) $p_{genotype}$ = 0.0173 (*)
				Šidák's multiple comparison post hoc test	$p_{WT\text{-}CTRL\ vs\ DKO\text{-}CTRL}$ = 0.0089 (**) $p_{WT\text{-}BDNF\ vs\ DKO\text{-}BDNF}$ = 0.0353 (*)
	mRNA expression of *Vgf* upon BDNF treatment	WT ± BDNF DKO ± BDNF	4 cultures	Two-way repeated measures ANOVA	$p_{treatment\ X\ genotype}$ = 0.2512 $p_{treatment}$ = 0.0059 (**) $p_{genotype}$ = 0.0179 (*)
				Šidák's multiple comparison post hoc test	$p_{WT\text{-}CTRL\ vs\ DKO\text{-}CTRL}$ = 0.0150 (*) $p_{WT\text{-}BDNF\ vs\ DKO\text{-}BDNF}$ = 0.0417 (*)
	mRNA expression of *Npy* upon BDNF treatment	WT ± BDNF DKO ± BDNF	4 cultures	Two-way repeated measures ANOVA	$p_{treatment\ X\ genotype}$ = 0.7666 $p_{treatment}$ = 0.1561 $p_{genotype}$ = 0.0335 (*)
				Šidák's multiple comparison post hoc test	$p_{WT\text{-}CTRL\ vs\ DKO\text{-}CTRL}$ = 0.0003 (***) $p_{WT\text{-}BDNF\ vs\ DKO\text{-}BDNF}$ = 0.0003 (***)
6H	mRNA expression of *Bdnf* (transcript isoform 1) upon overexpression (OE) of CREB (Y134F)	WT ± OE DKO ± OE	4 cultures	Two-way repeated measures ANOVA	$p_{treatment\ X\ genotype}$ = 0.0719 $p_{treatment}$ = 0.1192 $p_{genotype}$ = 0.0119 (*)
				Šidák's multiple comparison post hoc test	$p_{WT\text{-}CTRL\ vs\ DKO\text{-}CTRL}$ = 0.0316 (*) $p_{WT\text{-}OE\ vs\ DKO\text{-}OE}$ = 0.0062 (**)

	mRNA expression of *Vgf* upon overexpression (OE) of CREB (Y134F)	WT ± OE DKO ± OE	4 cultures	Two-way repeated measures ANOVA	$p_{treatment\ X\ genotype}$ = 0.1598 $p_{treatment}$ = 0.0035 (**) $p_{genotype}$ = 0.0098 (**)
				Šidák's multiple comparison post hoc test	$p_{WT\text{-}CTRL\ vs\ DKO\text{-}CTRL}$ = 0.0771 $p_{WT\text{-}OE\ vs\ DKO\text{-}OE}$ = 0.0173 (*)
6 suppl 1B	Band intensities of pCREB (S133) (WB)	DKO (% WT)	6 (6)	One sample t test (compare to 100%)	p = 0.0993

* n-number is the number of independent culture preparations. The number of individual observations is provided in brackets.

Materials availability

All DNA constructs and mouse models used in this study are available upon request. Requests should be directed to the lead contact, Matthijs Verhage (m.verhage@vu.nl).

Acknowledgements

We are indebted to D. Schut, L. Laan, I. Saarlos, R. Zalm, J. Wortel, J. Hoetjes, R. Dekker, I. Paliukhovich for their excellent technical assistance. This work was supported by the DFG (German Research Foundation) postdoctoral fellowship to A. Subkhangulova (DFG project number SU 1131/1-1).

Competing interests

The authors declare no competing interests.

602

603 **References**

604 Baba T, Sakisaka T, Mochida S & Takai Y (2005) PKA-catalyzed phosphorylation of tomosyn and
605 its implication in Ca2+-dependent exocytosis of neurotransmitter. *J Cell Biol* 170: 1113–
606 1125

607 Barak B, Williams A, Bielopolski N, Gottfried I, Okun E, Brown MA, Matti U, Rettig J, Stuenkel EL
608 & Ashery U (2010) Tomosyn Expression Pattern in the Mouse Hippocampus Suggests
609 Both Presynaptic and Postsynaptic Functions. *Front Neuroanat* 4

610 Ben-Simon Y, Rodenas-Ruano A, Alviña K, Lam AD, Stuenkel EL, Castillo PE & Ashery U (2015) A
611 Combined Optogenetic-Knockdown Strategy Reveals a Major Role of Tomosyn in Mossy
612 Fiber Synaptic Plasticity. *Cell Reports* 12: 396–404

613 Boncompain G, Divoux S, Gareil N, de Forges H, Lescure A, Latreche L, Mercanti V, Jollivet F,
614 Raposo G & Perez F (2012) Synchronization of secretory protein traffic in populations of
615 cells. *Nat Methods* 9: 493–498

616 Cazares VA, Njus MM, Manly A, Saldate JJ, Subramani A, Ben-Simon Y, Sutton MA, Ashery U &
617 Stuenkel EL (2016) Dynamic Partitioning of Synaptic Vesicle Pools by the SNARE-Binding
618 Protein Tomosyn. *J Neurosci* 36: 11208–11222

619 Chen K, Richlitzki A, Featherstone DE, Schwärzel M & Richmond JE (2011) Tomosyn-dependent
620 regulation of synaptic transmission is required for a late phase of associative odor
621 memory. *Proceedings of the National Academy of Sciences* 108: 18482–18487

622 Cheviet S, Bezzi P, Ivarsson R, Renström E, Viertl D, Kasas S, Catsicas S & Regazzi R (2006)
623 Tomosyn-1 is involved in a post-docking event required for pancreatic β-cell exocytosis. *J*
624 *Cell Sci* 119: 2912–2920

625 Ch'ng Q, Sieburth D & Kaplan JM (2008) Profiling Synaptic Proteins Identifies Regulators of
626 Insulin Secretion and Lifespan. *PLoS Genet* 4: e1000283

627 Cukier HN, Dueker ND, Slifer SH, Lee JM, Whitehead PL, Lalanne E, Leyva N, Konidari I, Gentry
628 RC, Hulme WF, *et al* (2014) Exome sequencing of extended families with autism reveals
629 genes shared across neurodevelopmental and neuropsychiatric disorders. *Molecular*
630 *Autism* 5: 1

631 De Rubeis S, He X, Goldberg AP, Poultney CS, Samocha K, Ercument Cicek A, Kou Y, Liu L, Fromer
632 M, Walker S, *et al* (2014) Synaptic, transcriptional and chromatin genes disrupted in
633 autism. *Nature* 515: 209–215

634 Demichev V, Messner CB, Vernardis SI, Lilley KS & Ralser M (2020) DIA-NN: neural networks and
635 interference correction enable deep proteome coverage in high throughput. *Nat*
636 *Methods* 17: 41–44

637 Dieni S, Matsumoto T, Dekkers M, Rauskolb S, Ionescu MS, Deogracias R, Gundelfinger ED,
638 Kojima M, Nestel S, Frotscher M, *et al* (2012) BDNF and its pro-peptide are stored in
639 presynaptic dense core vesicles in brain neurons. *J Cell Biol* 196: 775–788

640 Du K, Asahara H, Jhala US, Wagner BL & Montminy M (2000) Characterization of a CREB Gain-
641 of-Function Mutant with Constitutive Transcriptional Activity In Vivo. *Molecular and*
642 *Cellular Biology* 20: 4320–4327

643 Emperador-Melero J, Huson V, van Weering J, Bollmann C, Fischer von Mollard G, Toonen RF &
644 Verhage M (2018) Vti1a/b regulate synaptic vesicle and dense core vesicle secretion via
645 protein sorting at the Golgi. *Nat Commun* 9: 3421

646 Ernfors P, Bengzon J, Kokaia Z, Persson H & Lindvall O (1991) Increased levels of messenger
647 RNAs for neurotrophic factors in the brain during kindling epileptogenesis. *Neuron* 7:
648 165–176

649 Esvald E-E, Tuvikene J, Sirp A, Patil S, Bramham CR & Timmusk T (2020) CREB Family
650 Transcription Factors Are Major Mediators of BDNF Transcriptional Autoregulation in
651 Cortical Neurons. *J Neurosci* 40: 1405–1426

652 Finkbeiner S, Tavazoie SF, Maloratsky A, Jacobs KM, Harris KM & Greenberg ME (1997) CREB: A
653 Major Mediator of Neuronal Neurotrophin Responses. *Neuron* 19: 1031–1047

654 Forsmark A, Rossi G, Wadskog I, Brennwald P, Warringer J & Adler L (2011) Quantitative
655 Proteomics of Yeast Post-Golgi Vesicles Reveals a Discriminating Role for Sro7p in
656 Protein Secretion. *Traffic* 12: 740–753

657 Fujita Y, Shirataki H, Sakisaka T, Asakura T, Ohya T, Kotani H, Yokoyama S, Nishioka H, Matsuura
658 Y, Mizoguchi A, *et al* (1998) Tomosyn: a Syntaxin-1–Binding Protein that Forms a Novel
659 Complex in the Neurotransmitter Release Process. *Neuron* 20: 905–915

660 Ge SX, Jung D & Yao R (2020) ShinyGO: a graphical gene-set enrichment tool for animals and
661 plants. *Bioinformatics* 36: 2628–2629

662 Geerts CJ, Mancini R, Chen N, Koopmans FTW, Li KW, Smit AB, Weering JRT van, Verhage M &
663 Groffen AJA (2017) Tomosyn associates with secretory vesicles in neurons through its N-
664 and C-terminal domains. *PLOS ONE* 12: e0180912

665 Geerts CJ, Plomp JJ, Koopmans B, Loos M, van der Pijl EM, van der Valk MA, Verhage M &
666 Groffen AJA (2015) Tomosyn-2 is required for normal motor performance in mice and
667 sustains neurotransmission at motor endplates. *Brain Struct Funct* 220: 1971–1982

668 Gonzalez-Lozano MA & Koopmans F (2019) Data-Independent Acquisition (SWATH) Mass
669 Spectrometry Analysis of Protein Content in Primary Neuronal Cultures. In
670 *Neuroproteomics*, Li KW (ed) pp 119–127. New York, NY: Springer

671 Gonzalez-Lozano MA, Wortel J, van der Loo RJ, van Weering JRT, Smit AB & Li KW (2021)
672 Reduced mGluR5 Activity Modulates Mitochondrial Function. *Cells* 10: 1375

673 Gracheva EO, Burdina AO, Holgado AM, Berthelot-Grosjean M, Ackley BD, Hadwiger G, Nonet
674 ML, Weimer RM & Richmond JE (2006) Tomosyn Inhibits Synaptic Vesicle Priming in
675 Caenorhabditis elegans. *PLOS Biology* 4: e261

676 Gracheva EO, Burdina AO, Touroutine D, Berthelot-Grosjean M, Parekh H & Richmond JE (2007)
677 Tomosyn Negatively Regulates CAPS-Dependent Peptide Release at Caenorhabditis
678 elegans Synapses. *J Neurosci* 27: 10176–10184

679 Groffen AJA, Jacobsen L, Schut D & Verhage M (2005) Two distinct genes drive expression of
680 seven tomosyn isoforms in the mammalian brain, sharing a conserved structure with a
681 unique variable domain. *Journal of Neurochemistry* 92: 554–568

682 Hartmann M, Heumann R & Lessmann V (2001) Synaptic secretion of BDNF after high-
683 frequency stimulation of glutamatergic synapses. *EMBO J* 20: 5887–5897

684 Hatsuzawa K, Lang T, Fasshauer D, Bruns D & Jahn R (2003) The R-SNARE Motif of Tomosyn
685 Forms SNARE Core Complexes with Syntaxin 1 and SNAP-25 and Down-regulates
686 Exocytosis. *J Biol Chem* 278: 31159–31166

687 Hayashi T, McMahon H, Yamasaki S, Binz T, Hata Y, Südhof T c. & Niemann H (1994) Synaptic
688 vesicle membrane fusion complex: action of clostridial neurotoxins on assembly. *The*
689 *EMBO Journal* 13: 5051–5061

690 Hermel J-M, Dirkx Jr. R & Solimena M (1999) Post-translational modifications of ICA512, a
691 receptor tyrosine phosphatase-like protein of secretory granules. *European Journal of*
692 *Neuroscience* 11: 2609–2620

693 Isackson PJ, Huntsman MM, Murray KD & Gall CM (1991) BDNF mRNA expression is increased in
694 adult rat forebrain after limbic seizures: temporal patterns of induction distinct from
695 NGF. *Neuron* 6: 937–948

696 Jakobs MA, Dimitracopoulos A & Franze K (2019) KymoButler, a deep learning software for
697 automated kymograph analysis. *eLife* 8: e42288

698 Koopmans F, Li KW, Klaassen RV, Smit AB (2022) MS-DAP platform for downstream data
699 analysis of label-free proteomics uncovers optimal workflows in benchmark datasets
700 and increased sensitivity in analysis of Alzheimer's biomarker. *J Proteome*
701

702 Kumar R, Corbett MA, Smith NJC, Jolly LA, Tan C, Keating DJ, Duffield MD, Utsumi T, Moriya K,
703 Smith KR, *et al* (2015) Homozygous mutation of STXBP5L explains an autosomal
704 recessive infantile-onset neurodegenerative disorder. *Hum Mol Genet* 24: 2000–2010

705 Lee G & Saito I (1998) Role of nucleotide sequences of loxP spacer region in Cre-mediated
706 recombination. *Gene* 216: 55–65

707 Lehman K, Rossi G, Adamo JE & Brennwald P (1999) Yeast Homologues of Tomosyn and lethal
708 giant larvae Function in Exocytosis and Are Associated with the Plasma Membrane
709 Snare, Sec9. *The Journal of Cell Biology* 146: 125–140

710 MacArthur L & Eiden L (1996) Neuropeptide genes: Targets of activity-dependent signal
711 transduction. *Peptides* 17: 721–728

712 Mansvelder HD & Kits KS (2000) Calcium channels and the release of large dense core vesicles
713 from neuroendocrine cells: spatial organization and functional coupling. *Progress in*
714 *Neurobiology* 62: 427–441

715 Masuda ES, Huang BCB, Fisher JM, Luo Y & Scheller RH (1998) Tomosyn Binds t-SNARE Proteins
716 via a VAMP-like Coiled Coil. *Neuron* 21: 479–480

717 Matsunami N, Hadley D, Hensel CH, Christensen GB, Kim C, Frackelton E, Thomas K, Silva RP da,
718 Stevens J, Baird L, *et al* (2013) Identification of Rare Recurrent Copy Number Variants in
719 High-Risk Autism Families and Their Prevalence in a Large ASD Population. *PLOS ONE* 8:
720 e52239

721 McEwen JM, Madison JM, Dybbs M & Kaplan JM (2006) Antagonistic Regulation of Synaptic
722 Vesicle Priming by Tomosyn and UNC-13. *Neuron* 51: 303–315

723 Moore AN, Waxham MN & Dash PK (1996) Neuronal Activity Increases the Phosphorylation of
724 the Transcription Factor cAMP Response Element-binding Protein (CREB) in Rat
725 Hippocampus and Cortex*. *Journal of Biological Chemistry* 271: 14214–14220

726 Moro A, van Nifterick A, Toonen RF & Verhage M (2021) Dynamin controls neuropeptide
727 secretion by organizing dense-core vesicle fusion sites. *Sci Adv* 7: eabf0659

728 Moro A, Woerden GM van, Toonen RF & Verhage M (2020) CaMKII controls neuromodulation
729 via neuropeptide gene expression and axonal targeting of neuropeptide vesicles. *PLOS*
730 *Biology* 18: e3000826

731 Nassal JP, Murphy FH, Toonen RF & Verhage M (2022) Differential axonal trafficking of
732 Neuropeptide Y-, LAMP1-, and RAB7-tagged organelles in vivo. *eLife* 11: e81721

733 Nusbaum MP, Blitz DM & Marder E (2017) Functional consequences of neuropeptide and small-
734 molecule co-transmission. *Nat Rev Neurosci* 18: 389–403

735 Otto H, Hanson PI & Jahn R (1997) Assembly and disassembly of a ternary complex of
736 synaptobrevin, syntaxin, and SNAP-25 in the membrane of synaptic vesicles. *Proceedings*
737 *of the National Academy of Sciences* 94: 6197–6201

738 Persoon CM, Hoogstraaten RI, Nassal JP, van Weering JRT, Kaeser PS, Toonen RF & Verhage M
739 (2019) The RAB3-RIM Pathway Is Essential for the Release of Neuromodulators. *Neuron*
740 104: 1065-1080.e12

741 Persoon CM, Moro A, Nassal JP, Farina M, Broeke JH, Arora S, Dominguez N, van Weering JR,
742 Toonen RF & Verhage M (2018) Pool size estimations for dense-core vesicles in
743 mammalian CNS neurons. *The EMBO Journal*: 18

744 Pobbati AV, Razeto A, Böddener M, Becker S & Fasshauer D (2004) Structural Basis for the
745 Inhibitory Role of Tomosyn in Exocytosis. *J Biol Chem* 279: 47192–47200

746 Quassollo G, Wojnacki J, Salas DA, Gastaldi L, Marzolo MP, Conde C, Bisbal M, Couve A &
747 Cáceres A (2015) A RhoA Signaling Pathway Regulates Dendritic Golgi Outpost
748 Formation. *Current Biology* 25: 971–982

749 Rizo J & Xu J (2015) The Synaptic Vesicle Release Machinery. *Annual Review of Biophysics* 44:
750 339–367

751 Rossi G, Watson K, Kennedy W & Brennwald P (2018) The tomosyn homologue, Sro7, is a direct
752 effector of the Rab GTPase, Sec4, in post-Golgi vesicle tethering. *MBoC* 29: 1476–1486

753 Sakisaka T, Yamamoto Y, Mochida S, Nakamura M, Nishikawa K, Ishizaki H, Okamoto-Tanaka M,
754 Miyoshi J, Fujiyoshi Y, Manabe T, *et al* (2008) Dual inhibition of SNARE complex
755 formation by tomosyn ensures controlled neurotransmitter release. *The Journal of Cell*
756 *Biology* 183: 323–337

757 Saunders A, Macosko EZ, Wysoker A, Goldman M, Krienen FM, de Rivera H, Bien E, Baum M,
758 Bortolin L, Wang S, *et al* (2018) Molecular Diversity and Specializations among the Cells
759 of the Adult Mouse Brain. *Cell* 174: 1015-1030.e16

760 Sauvola CW, Akbergenova Y, Cunningham KL, Aponte-Santiago NA & Littleton JT (2021) The
761 decoy SNARE Tomosyn sets tonic versus phasic release properties and is required for
762 homeostatic synaptic plasticity. *eLife* 10: e72841

763 Scalettar BA (2006) How Neurosecretory Vesicles Release Their Cargo. *Neuroscientist* 12: 164–
764 176

765 Schindelin J, Arganda-Carreras I, Frise E, Kaynig V, Longair M, Pietzsch T, Preibisch S, Rueden C,
766 Saalfeld S, Schmid B, *et al* (2012) Fiji: an open-source platform for biological-image
767 analysis. *Nat Methods* 9: 676–682

768 Sengupta D & Linstedt AD (2011) Control of Organelle Size: The Golgi Complex. *Annu Rev Cell*
769 *Dev Biol* 27: 57–77

770 Shen W, Kilander MBC, Bridi MS, Frei JA, Niescier RF, Huang S & Lin Y (2020) Tomosyn regulates
771 the small RhoA GTPase to control the dendritic stability of neurons and the surface
772 expression of AMPA receptors. *J Neurosci Res* 98: 1213–1231

773 Sorra KE, Mishra A, Kirov SA & Harris KM (2006) Dense core vesicles resemble active-zone
774 transport vesicles and are diminished following synaptogenesis in mature hippocampal
775 slices. *Neuroscience* 141: 2097–2106

776 Südhof TC (2013) Neurotransmitter Release: The Last Millisecond in the Life of a Synaptic
777 Vesicle. *Neuron* 80: 675–690

778 Takamori S, Holt M, Stenius K, Lemke EA, Grønborg M, Riedel D, Urlaub H, Schenck S, Brügger B,
779 Ringler P, *et al* (2006) Molecular Anatomy of a Trafficking Organelle. *Cell* 127: 831–846

780 Tao X, Finkbeiner S, Arnold DB, Shaywitz AJ & Greenberg ME (1998) Ca2+ Influx Regulates BDNF
781 Transcription by a CREB Family Transcription Factor-Dependent Mechanism. *Neuron* 20:
782 709–726

783 Wegrzyn JL, Bark SJ, Funkelstein L, Mosier C, Yap A, Kazemi-Esfarjani P, La Spada AR, Sigurdson
784 C, O'Connor DT & Hook V (2010) Proteomics of Dense Core Secretory Vesicles Reveal
785 Distinct Protein Categories for Secretion of Neuroeffectors for Cell−Cell Communication.
786 *J Proteome Res* 9: 5002–5024

787 van Westen R, Poppinga J, Díez Arazola R, Toonen RF & Verhage M (2021) Neuromodulator
788 release in neurons requires two functionally redundant calcium sensors. *Proceedings of*
789 *the National Academy of Sciences* 118: e2012137118

790 Wolzak K, Nölle A, Farina M, Abbink TE, van der Knaap MS, Verhage M & Scheper W (2022)
791 Neuron-specific translational control shift ensures proteostatic resilience during ER
792 stress. *The EMBO Journal* 41: e110501

793 Xia X, Lessmann V & Martin TFJ (2009) Imaging of evoked dense-core-vesicle exocytosis in
794 hippocampal neurons reveals long latencies and kiss-and-run fusion events. *J Cell Sci*
795 122: 75–82

796 Ye S, Huang Y, Joshi S, Zhang J, Yang F, Zhang G, Smyth SS, Li Z, Takai Y & Whiteheart SW (2014)
797 Platelet secretion and hemostasis require syntaxin-binding protein STXBP5. *J Clin Invest*
798 124: 4517–4528

799 Yizhar O, Matti U, Melamed R, Hagalili Y, Bruns D, Rettig J & Ashery U (2004) Tomosyn inhibits
800 priming of large dense-core vesicles in a calcium-dependent manner. *PNAS* 101: 2578–
801 2583

802 Zafra F, Hengerer B, Leibrock J, Thoenen H & Lindholm D (1990) Activity dependent regulation
803 of BDNF and NGF mRNAs in the rat hippocampus is mediated by non-NMDA glutamate
804 receptors. *EMBO J* 9: 3545–3550

805 Zhu Q, Yamakuchi M, Ture S, Garcia-Hernandez M de la L, Ko KA, Modjeski KL, LoMonaco MB,
806 Johnson AD, O'Donnell CJ, Takai Y, *et al* (2014) Syntaxin-binding protein STXBP5 inhibits
807 endothelial exocytosis and promotes platelet secretion. *J Clin Invest* 124: 4503–4516

808 Zupanc GKH (1996) Peptidergic transmission: From morphological correlates to functional
809 implications. *Micron* 27: 35–91

810

811

Figure legends

Figure 1

Loss of tomosyns does not affect fusion of DCVs in mouse hippocampal neurons.

(A) Experimental strategy for measuring DCV fusion in single isolated neurons. Results of the experiment are shown in (B-E).

(B) Cumulative count of fusion events detected per single neuron. Blue lines indicate time of electric stimulation (16 bursts of 50 pulses at 50 Hz each). Data are shown as mean ± SEM and were analyzed by two-way ANOVA. n=34-36 neurons/ genotype from three culture preparations.

(C) Total count of fusion events detected per single neuron. Data are shown as violin plot with median (dashed line) and quartiles (dotted lines) and analyzed using Mann-Whitney test.

(D) Intracellular pool of pHluorin-labeled DCVs determined by application of 50 mM NH_4Cl after the stimulation. Data are shown as violin plot with median (dashed line) and quartiles (dotted lines) and analyzed using a two-tailed unpaired *t*-test. $^{*}p < 0.05$.

(E) Cumulative count of fusion events normalized to the intracellular pool of DCVs (release fraction). Data are shown as mean ± SEM and were analyzed by two-way ANOVA.

(F) Peak in fluorescence intensity that results from a single fusion event (averaged per neuron). Data are shown as violin plot with median (dashed line) and quartiles (dotted lines) and analyzed using Mann-Whitney test. ns: not significant.

(G) Levels of syntaxin-1 containing 80 kDa SNARE complexes are unchanged in DKO neurons. Boiled and non-boiled lysates were subjected to SDS-PAGE and membranes were probed with an antibody against syntaxin-1 (STX1). Temperature-sensitive complexes were detected at 80 kDa (synaptic SNARE complex) and 200 kDa (possibly complex of syntaxin-1 and SNAP25 with tomosyn). Smear at >80 kDa represents complex multimers. Band intensities in DKO were normalized to WT, plotted as mean ± SD and analyzed using a one sample *t*-test. Dots represent independent culture preparations (n=4). ns: not significant; $^{***}p < 0.001$.

(H) DCV reporter levels are reduced in DKO neurons silenced with the sodium channel blocker tetrodotoxin (TTX). Representative images of NPY-pHluorin in fixed WT and DKO neurons are shown. Neurons were grown in network (mass) cultures, treated with 1 µM TTX for 48 hours, and fixed on DIV14 before imaging. Scale bar 20 µm.

(I) Mean intensity of the DCV reporter in neurites and somas of silenced WT and DKO neurons exemplified in (H). Data are shown as mean ± SD and were analyzed using a two-tailed unpaired *t*-test with Welch's correction. n=23-24 neurons/ genotype. Dots represent individual neurons. $^{**}p < 0.01$, $^{****}p < 0.0001$.

Figure 1 supplement 1

Validation of the mouse model with the conditional deletion of tomosyn and tomosyn-2.

849 (A) Schematic depiction of mouse *Stxbp5* (encoding tomosyn) and *Stxbp5l* (encoding tomosyn-
850 2) genes with exons as vertical lines and introns as bridging gaps. To generate conditional
851 double knockout (DKO) of *Stxbp5/5l*, exon 2 of *Stxbp5* and exon 3 of *Stxbp5l* were flanked with
852 Lox2272 and LoxP sites, respectively (shown as triangles). Expression of Cre-recombinase
853 results in excision of the flanked exons in both genes, predicted to cause frameshift mutations
854 and nonsense-mediated mRNA decay of gene transcripts. Proportional gene graphics were
855 made using Exon-Intron Graphic Maker developed by Nikhil Bhatla.

856 (B) Western blot showing loss of tomosyn and tomosyn-2 expression in Cre-expressing primary
857 hippocampal neurons ('DKO'). As control ('WT'), neurons expressing Cre lacking the DNA-
858 binding domain (ΔCre) were used. Arrow indicates tomosyn, which is flanked by two unspecific
859 bands. Numbers on the left indicate approximate molecular weight of the bands in kDa.

860 (C) Immunostaining of tomosyn and MAP2 showing loss of tomosyn expression in DKO neurons.
861 Scale bar 20 µm.

862 (D) Example cropped images of WT and DKO neurons immunostained for the synaptic marker
863 synaptophysin ('SYP') showing normal synapse number and distribution in the KO neurons
864 (quantified in E-G). Scale bar 20 µm.

865 (E) Total length of MAP2-positive neurites per single neuron.

866 (F) Number of synaptophysin puncta normalized to length of MAP2-positive neurites.

867 (G) Mean intensity of synaptophysin signal on MAP2-positive neurites.

868 Data in E-G are shown as mean ± SD and were analyzed using a two-tailed unpaired *t*-test.
869 n=28-30 neurons/ genotype. ns: not significant.

870

871 **Figure 1 supplement 2**
872 **Design and validation of the pHluorin-based DCV fusion reporter.**

873 (A) DCV fusion reporter used in this study is based on the human pre-pro-NPY (NPY precursor),
874 which structure is shown in the upper panel with processing sites depicted as scissors. In the
875 DCV fusion reporter, C-flanking peptide (aa 64-97) was replaced by super-ecliptic pHluorin.

876 (B) DCV fusion reporter localizes to endogenous DCVs in cultured neurons, as shown by co-
877 localization of pre-NPY-pHluorin with the endogenous DCV markers IA-2, chromogranin A
878 (CHGA) and chromogranin B (CHGB). White frames indicate zoomed areas used to generate
879 intensity profiles shown on the right. Scale bar 20 µm.

880

881 **Figure 1 supplement 3**
882 **Expression of EGFP under control of synapsin promoter is not affected in DKO neurons.**

883 (A) Representative images of EGFP expressed under control of synapsin promoter in fixed WT
884 and DKO neurons. Scale bar 20 µm.

885 (B) Quantification of the mean EGFP intensity in WT and DKO neurons from confocal
886 microscopy images as exemplified in (A). Data are shown as mean ± SD and were analyzed using
887 a two-tailed unpaired *t*-test. n=28-30 neurons/ genotype. ns: not significant.

888

889 **Figure 2**
890 **Tomosyns regulate number and/ or composition of neuronal DCVs.**

891 (A) BDNF levels are decreased in DKO neurons. Representative images of BDNF immunostaining
892 in single DIV21 neurons grown on glia microislands. White boxes indicate a zoomed view of the
893 neurites with BDNF puncta. Scale bar 20 µm.

894 (B) Quantification of the mean BDNF intensity in WT and DKO neurons from confocal
895 microscopy images exemplified in (A). Data are shown as mean ± SD and were analyzed using a
896 two-tailed unpaired *t*-test. n=32-35 neurons/ genotype from three culture preparations. ****$p <$
897 0.0001.

898 (C) Levels of a DCV-resident protein IA-2 (PTPRN) are decreased in DKO neurons.
899 Representative images of the IA-2 immunostaining in DIV14 neurons. White boxes indicate a
900 zoomed view on the neurites with IA-2 puncta. Scale bar 20 µm.

901 (D) Quantification of the mean IA-2 intensity in WT and DKO neurons from confocal microscopy
902 images exemplified in (D). Data are shown as mean ± SD and were analyzed using a two-tailed
903 unpaired *t*-test. n=24 neurons/ genotype. *$p < 0.05$; ****$p < 0.0001$.

904 (E) Levels of IA-2 as detected by WB are decreased in DKO neurons. Proteolytically processed
905 (mature) form of IA-2 was detected at 65 kDa. Equal loading was verified by the detection of
906 total protein stained with trichloroethanol (TCE) and by immunodetection of actin. Amount of
907 mature IA-2 in DKO neurons was normalized to WT levels in the corresponding culture. DKO
908 data are presented as mean ± SD and were analyzed using one sample *t*-test. n=9 samples/
909 genotype from three culture preparations. ****$p < 0.0001$.

910

911 **Figure 2 supplement 1**
912 **Loss of tomosyns does not affect levels of endo-lysosomal proteins.**

913 (A) Representative images of LAMP1 immunostaining in DIV14 neurons. Scale bar 20 µm.

914 (B) Quantification of the mean LAMP1 intensity in WT and DKO neurons from confocal
915 microscopy images as exemplified in (A). Data are shown as mean ± SD and were analyzed using
916 a two-tailed unpaired *t*-test. n=10 neurons/ genotype. ns: not significant.

917 (C) Levels of LAMP1 and LIMP2 as detected by WB are normal in DKO neurons. Equal loading
918 was verified by immunodetection of actin.

919 (D) Quantification of LAMP1 and LIMP2 signal from WB images exemplified in (C). Levels of
920 LAMP1 and LIMP2 in DKO were normalized to WT levels in the corresponding culture. DKO data
921 are presented as mean ± SD and were analyzed using one sample *t*-test. n=9 samples/ genotype
922 from three culture preparations. ns: not significant.

923

924 **Figure 3**

925 **Proteomic analysis shows downregulation of DCV and cytoskeletal proteins in DKO neurons.**

926 (A) Volcano plot showing results of the differential expression analysis of WT and DKO
927 proteome. Grey lines indicate chosen thresholds for log2 fold change (0.3) and false discovery
928 (FDR) adjusted *p*-value (0.01). Proteins decreased or increased in DKO are shown in blue and
929 red, respectively.

930 (B) Enriched gene ontology (GO cellular component) terms of the proteins significantly affected
931 in DKO neurons as analyzed by ShinyGO v0.75 (http://bioinformatics.sdstate.edu/go/) with the
932 FDR-adjusted *p*-value cutoff ≤ 0.05.

933 (C) List of proteins reliably detected in one of the genotypes only, and therefore not included in
934 the differential expression analysis shown in (A). Proteins are sorted by the z-score, which
935 reflects the total number of peptides detected per genotype.

936 (D) Examples of proteins that are significantly affected in DKO neurons grouped by subcellular
937 compartment. Heat maps show the degree of down- or upregulation in the DKO.

938

939 **Figure 4**

940 **Loss of tomosyns results in a decrease of DCV but not of SV size.**

941 (A) Example EM images show normal appearance of DCVs with a typical dense core in DKO
942 neurons. Scale bar 100 nm.

943 (B) DCV diameter is reduced in DKO neurons, as quantified from EM images exemplified in (A).
944 Data are shown as a SuperPlot, where averages from three independent cultures (biological
945 replicates) are shown as large circles and single observations (DCV profiles) as dots. Data from
946 each culture are shown in different color. Horizontal bars represent means of the averages
947 from the three cultures, which were compared using a two-tailed unpaired *t*-test. Error bars are
948 SD. Number of DCV profiles analyzed: 135 (WT) and 64 (DKO). $*p < 0.05$.

949 (C) Frequency distribution of DCVs by diameter is skewed to the left in DKO neurons, indicating
950 a higher proportion of smaller DCVs in DKO neurons than in WT.

951 (D) Example EM images show normal ultrastructure of synapses and other cellular organelles in
952 DKO neurons. Golgi cisternae and selected mitochondria are labeled with 'G' and 'M',
953 respectively. Scale bar 100 nm.

954 (E-H) Quantification of SV diameter, SV number per synapse, length of the active zone, and
955 length of postsynaptic density (PSD) from EM images exemplified in (D). Data are shown as
956 SuperPlots and analyzed as described in (B). Number of individual observations: 617-621 SV
957 profiles (E) and 148-152 synapses (F-H). ns: not significant.

958

959 **Figure 5**

960 **Loss of tomosyns results in the accelerated trafficking of a DCV cargo through Golgi.**

961 (A) TGN area is decreased in DKO neurons. Representative images of immunostained TGN
962 marker, TMEM87A (shown in cyan). Nuclei are labeled in red due to expression of mCherry-
963 tagged Cre or ΔCre. Scale bar 20 µm.

964 (B) Quantification of the area of the TGN and nuclei from confocal microscopy images
965 exemplified in (A). Data are shown as mean ± SD and were analyzed using a two-tailed unpaired
966 *t*-test. n=39-40 neurons/ genotype. $^{***}p < 0.001$; ns: not significant.

967 (C) Design of the construct for the RUSH assay. As a DCV cargo, human pre-pro-NPY fused to
968 SBP and EGFP was used. The cargo was immobilized at the ER due to interaction with the ER
969 hook, consisting of streptavidin fused to the ER-retention/ retrieval signal KDEL.

970 (D) Scheme illustrating synchronized trafficking of a DCV cargo through the secretory pathway
971 upon addition of biotin in the RUSH assay.

972 (E) Snapshots of time-lapse videos taken after addition of biotin in the RUSH assay. Time passed
973 after addition of biotin is shown on top. DCV cargo passes through the Golgi in roughly 45
974 minutes after addition of biotin and gets concentrated in fine puncta that eventually leave cell
975 soma. Scale bar 20 µm.

976 (F) NPY-EGFP intensity in the Golgi area plotted against time after addition of biotin. Intensity
977 values were normalized to the basal levels (before addition of biotin). Data are shown as mean
978 ± SEM and were analyzed by two-way ANOVA. n=30-34 neurons/ genotype.

979 (G) Time required to reach maximum NPY-EGFP intensity at the Golgi, quantified from (F), is
980 reduced in DKO. Data are shown as mean ± SD and were analyzed by a two-tailed unpaired *t*-
981 test. $^{*}p < 0.05$.

982 (H) Speed of NPY-EGFP export from the Golgi is increased in DKO neurons. Rate constants were
983 calculated from first order decay curves fitted to the data shown in (F). Data are shown as mean
984 ± SD and were analyzed by a two-tailed unpaired *t*-test. $^{*}p < 0.05$.

985 (I) Snapshots of time-lapse videos taken 90 min after addition of biotin in the RUSH assay with
986 the focus on neurites, where newly made DCVs trafficked after exit from the Golgi.

987 (J) Proportion of newly made DCVs trafficking in anterograde and retrograde directions as
988 quantified from the time-lapse videos exemplified in (I). Majority of vesicles trafficked
989 anterogradely in neurons of both genotypes. Data are shown as mean ± SD and were analyzed
990 by a two-tailed unpaired *t*-test. n=12 neurons/ genotype. ns: not significant.

991 (K) Speed of anterogradely trafficking vesicles as quantified from the time-lapse videos
992 exemplified in (I). Data are shown as mean ± SD and were analyzed by a two-tailed unpaired *t*-
993 test. n=12 neurons/ genotype. ns: not significant.

994

995 **Figure 5 supplement 1**
996 **Tomosyn localizes to the TGN.**

997 (A) Example confocal microscopy images showing partial co-localization of tomosyn with the
998 TGN marker, TGN38. Scale bar 20 µm.

(B) Intensity profile generated from the yellow line indicated in (A) showing partial colocalization of tomosyn and TGN38.

Figure 5 supplement 2
RUSH-generated vesicles contain endogenous DCV marker, CHGA.

Example confocal microscopy images showing co-localization of NPY-EGFP-SBP with CHGA. Scale bar 5 µm.

Figure 5 video 1
Live imaging of DCV formation in the RUSH assay.

Neurons expressing a DCV cargo (NPY -EGFP-SBP) and an ER hook (Streptavidin-KDEL) were imaged live upon addition of 40 µM biotin to the conditioned medium. Neurons were illuminated for 115 min with 488 nm laser at a frequency of 1 frame/ 5 min. Addition of biotin caused re-localization of NPY-EGFP-SBP signal from the ER to the Golgi and subsequently to post-Golgi vesicles. Scale bar 10 µm.

Figure 6
Gene expression of multiple DCV cargos is decreased in DKO neurons.

(A) Schematic representation of mouse *Bdnf* gene structure showing nine alternative promoter regions giving rise to multiple transcript isoforms, among which isoforms 1, 2, 4, 6 and 9 are most abundant in the hippocampus.

(B) mRNA levels of different *Bdnf* transcript isoforms as assessed by quantitative RT-PCR and normalized to *Gapdh*. Data are shown as fold changes (FC) relative to WT levels in the corresponding culture preparation. n=8 culture preparations/ genotype. Dots represent individual cultures, bar graphs are geometric means, error bars are geometric SD. Log2FC (ΔΔCt) were analyzed by one-sample *t*-test. $^{**}p < 0.01$; $^{***}p < 0.001$.

(C) mRNA levels of general DCV cargos as assessed by quantitative RT-PCR and normalized to *Gapdh*. Data are shown and analyzed as described in (B). $^{*}p < 0.05$; $^{**}p < 0.01$; $^{***}p < 0.001$.

(D) mRNA levels of most abundant hippocampal neuropeptides as assessed by quantitative RT-PCR and normalized to *Gapdh*. Neuropeptides are sorted by their abundance in hippocampal neurons. Data are shown and analyzed as described in (B). $^{*}p < 0.05$; $^{**}p < 0.01$; $^{***}p < 0.001$, ns: not significant.

(E) Scheme depicting a function of BDNF in regulating transcription of its own gene, as well as of other genes (e.g., *Vgf*), which, at least in part, is mediated by the transcription factor CREB.

(F) mRNA levels of *Bdnf*, *Vgf* and *Npy* upon treatment of cultured neurons with recombinant BDNF (50 ng/ml, 3h). The treatment results in an increase of *Bdnf* and *Vgf* mRNA levels in both genotypes (two-way ANOVA $p_{\text{treatment}} < 0.05$) but does not rescue the decreased mRNA levels in DKO (red bars). Data are shown as FC relative to untreated WT in the corresponding culture

1037 preparation. n=4 culture preparations/ genotype. Dots represent independent culture
1038 preparations; bar graphs are geometric means. Log2FC (ΔΔCt) were analyzed by repeated
1039 measures two-way ANOVA with post hoc Šidák's multiple comparisons test. $^{*}p < 0.05$; $^{**}p <$
1040 0.01; $^{***}p < 0.001$.

1041 (G) Validation of the expression of CREB (Y134), a constitutively active form of CREB, by ICC in
1042 neurons transduced with CREB (Y134)-encoding lentivirus. Immunostaining of CREB
1043 phosphorylated at S133 is shown in green, MAP2 is shown in red. Scale bar 20 µm.

1044 (H) Overexpression of CREB (Y134) does not rescue reduced mRNA levels of *Bdnf* and *Vgf* in
1045 DKO neurons. Data are shown and analyzed as described in (F). $^{*}p < 0.05$; $^{**}p < 0.01$.

1046

1047 **Figure 6 supplement 1**
1048 **Levels of activated CREB are not affected in DKO neurons.**

1049 (A) Levels of CREB phosphorylated at S133 as detected by WB are normal in DKO neurons. Equal
1050 loading was verified by immunodetection of actin.

1051 (B) Quantification of pCREB signal from WB images exemplified in (A). Levels of pCREB in DKO
1052 were normalized to WT levels in the corresponding culture. DKO data are presented as mean ±
1053 SD and were analyzed using one sample *t*-test. n=6 samples/ genotype from six independent
1054 cultures. ns: not significant.

1055

1056

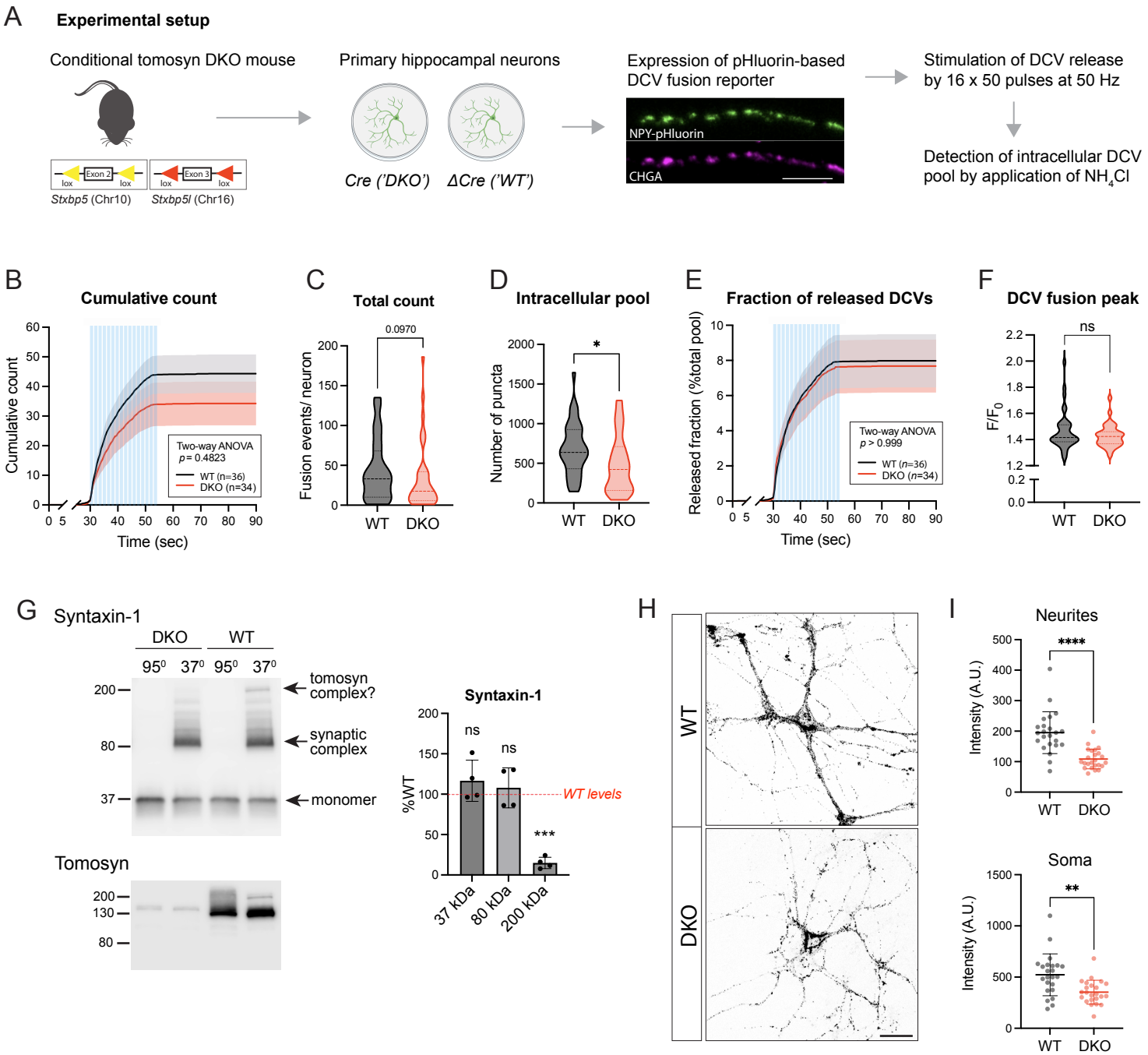
A
Experimental setup
Conditional tomosyn DKO mouse
Exon 2
lox
Stxbp5 (Chr10)
Exon 3
Stxbp5l (Chr16)
Primary hippocampal neurons
Cre ('DKO')
ΔCre ('WT')
Expression of pHluorin-based DCV fusion reporter
NPY-pHluorin
CHGA
Stimulation of DCV release by 16 x 50 pulses at 50 Hz
Detection of intracellular DCV pool by application of NH4Cl
B
Cumulative count
Cumulative count
Time (sec)
Two-way ANOVA
p = 0.4823
WT (n=36)
DKO (n=34)
C
Total count
Fusion events/ neuron
0.0970
WT
DKO
D
Intracellular pool
Number of puncta
*
WT
DKO
E
Fraction of released DCVs
Released fraction (%total pool)
Time (sec)
Two-way ANOVA
p > 0.999
WT (n=36)
DKO (n=34)
F
DCV fusion peak
F/F0
ns
WT
DKO
G
Syntaxin-1
DKO
WT
95⁰ 37⁰ 95⁰ 37⁰
200
80
37
tomosyn complex?
synaptic complex
monomer
Tomosyn
200
130
80
Syntaxin-1
%WT
ns
ns
***
WT levels
37 kDa
80 kDa
200 kDa
H
WT
DKO
I
Neurites
Intensity (A.U.)
****
WT
DKO
Soma
Intensity (A.U.)
**
WT
DKO

Figure 1

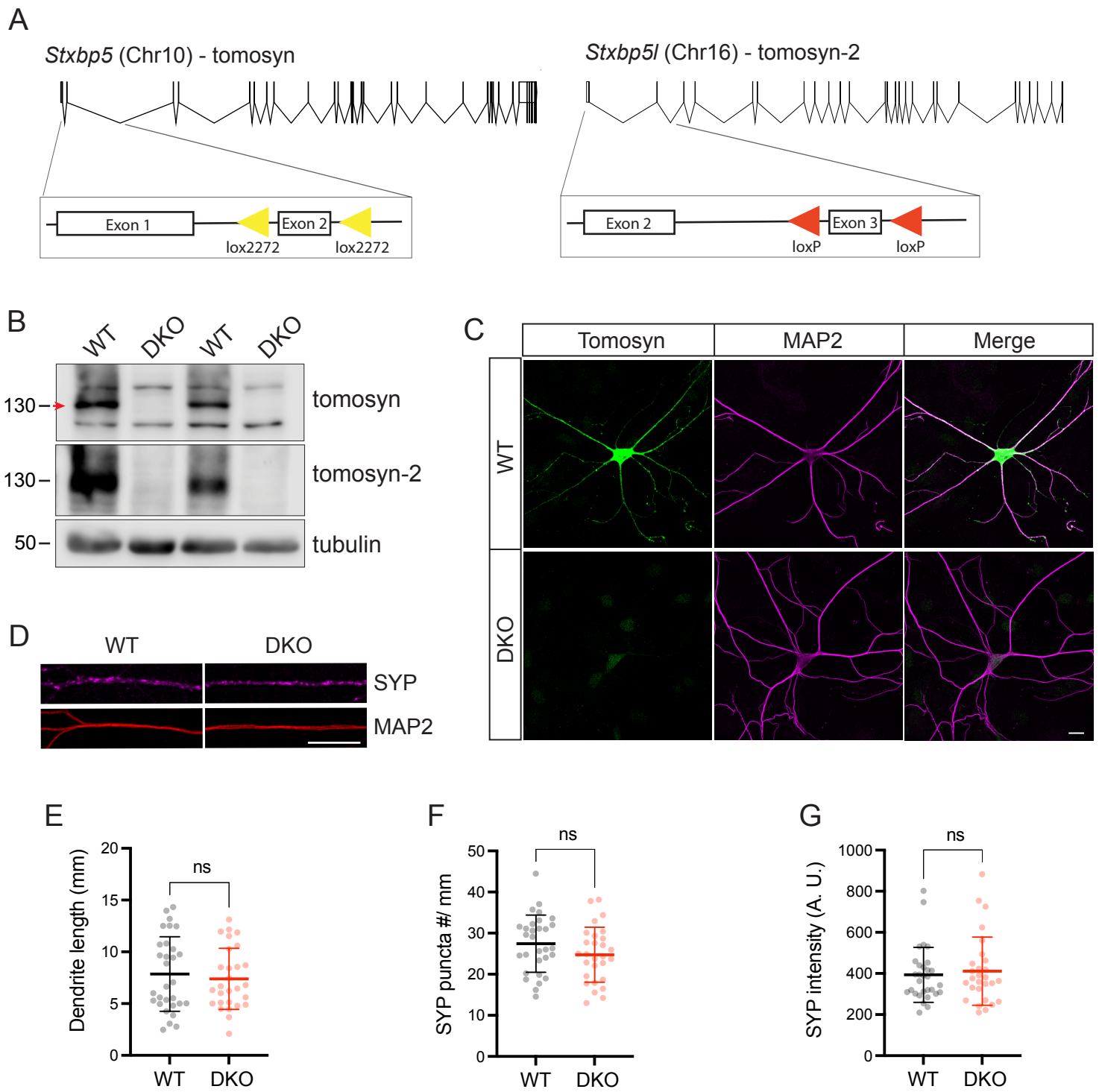

Figure 1–figure supplement 1

A

Design of the DCV reporter

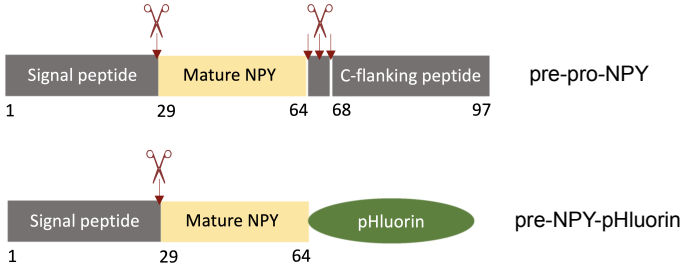

B

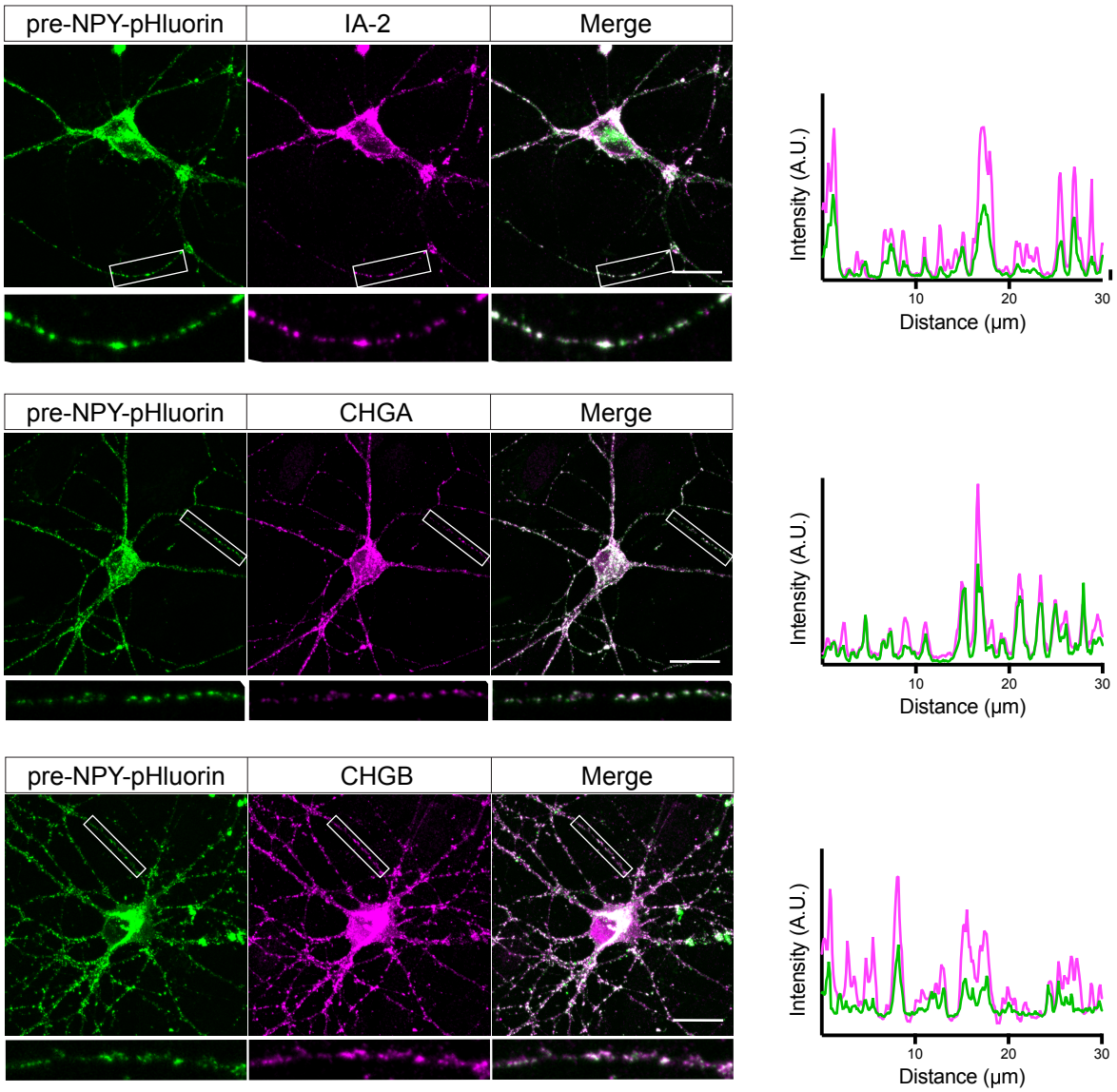

Figure 1–figure supplement 2

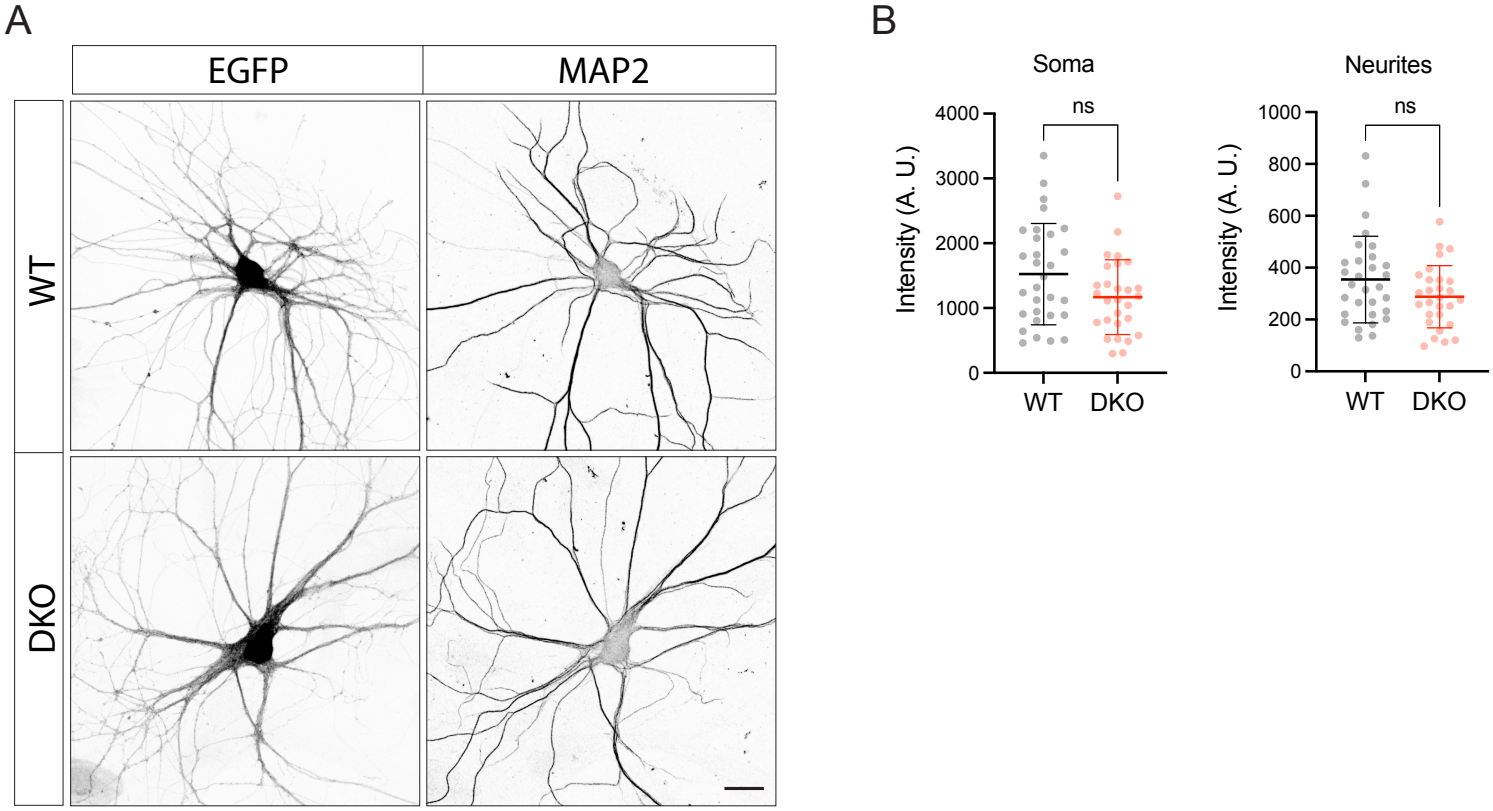

Figure 1–figure supplement 3

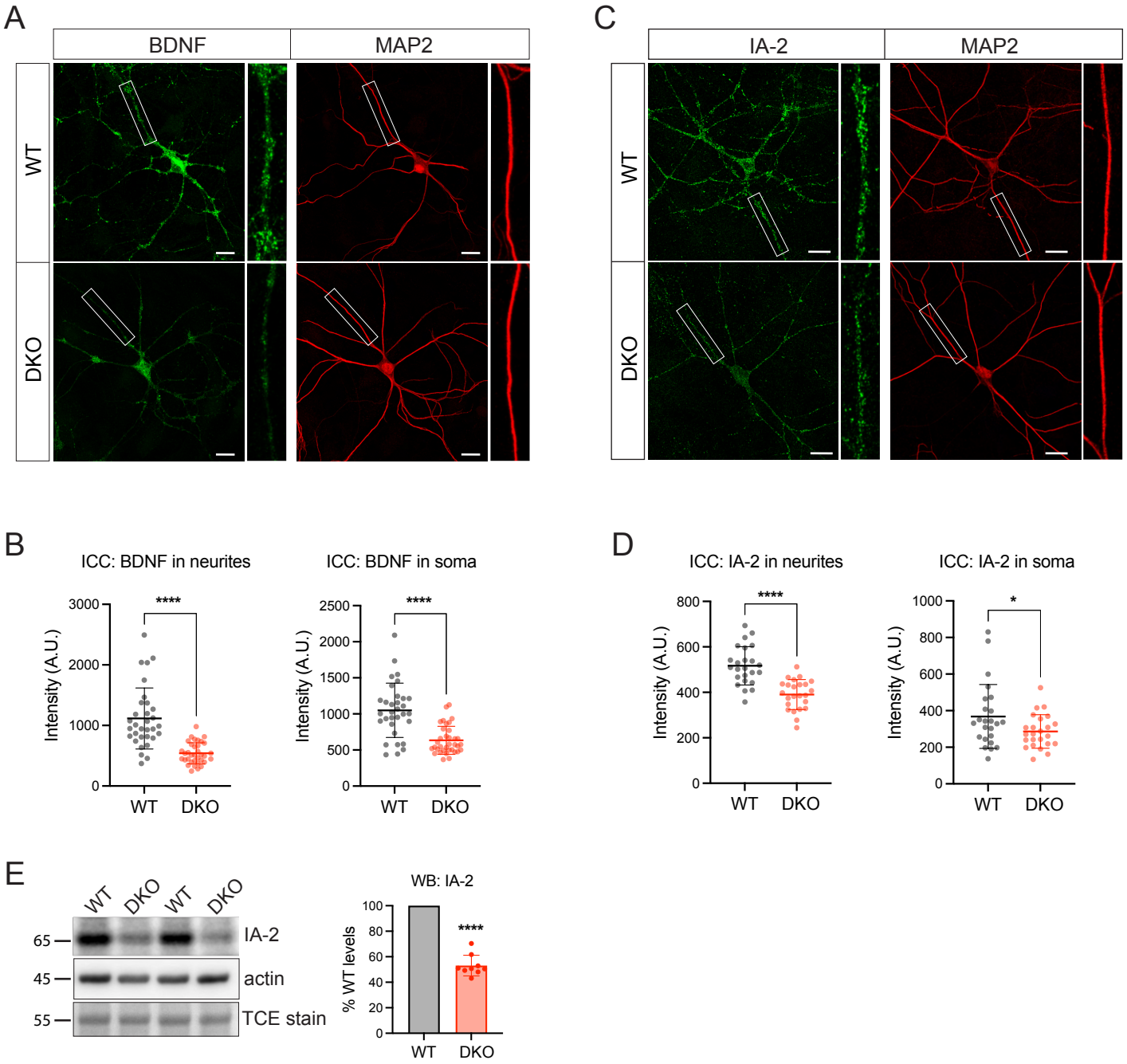
A
BDNF
MAP2
WT
DKO
C
IA-2
MAP2
WT
DKO
B
ICC: BDNF in neurites
ICC: BDNF in soma
Intensity (A.U.)
****
WT
DKO
D
ICC: IA-2 in neurites
ICC: IA-2 in soma
Intensity (A.U.)
****
*
WT
DKO
E
WT
DKO
WT
DKO
65
45
55
IA-2
actin
TCE stain
WB: IA-2
% WT levels
****
WT
DKO

Figure 2

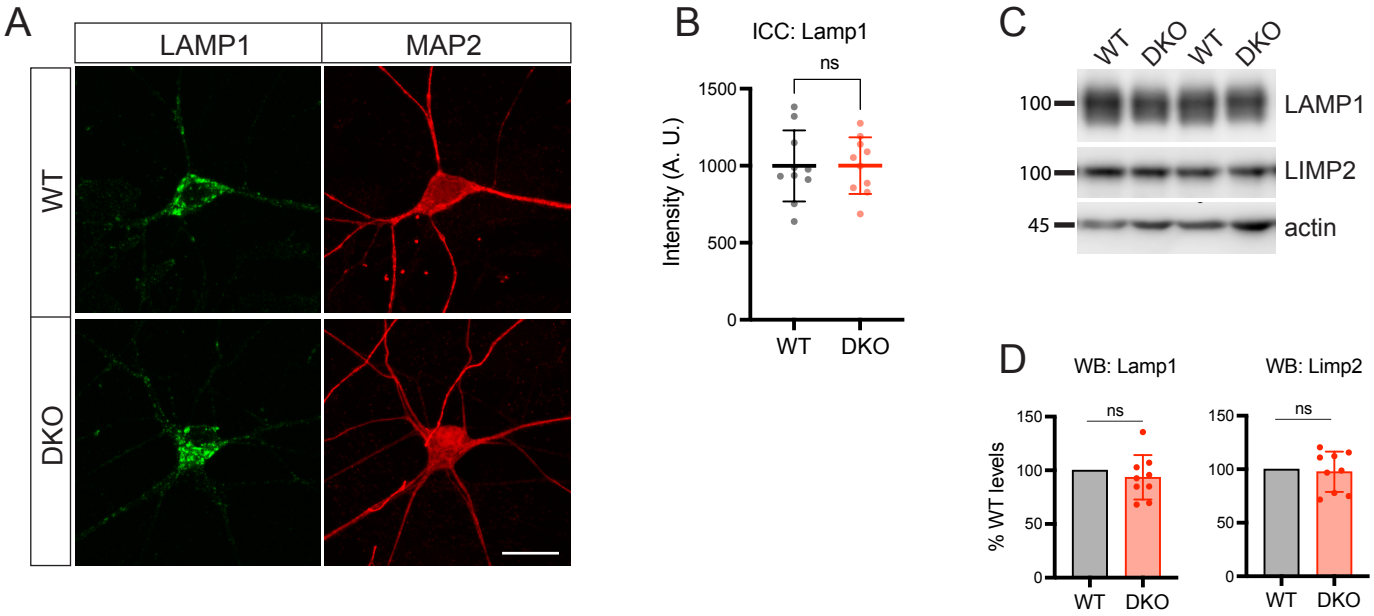

Figure 2–figure supplement 1

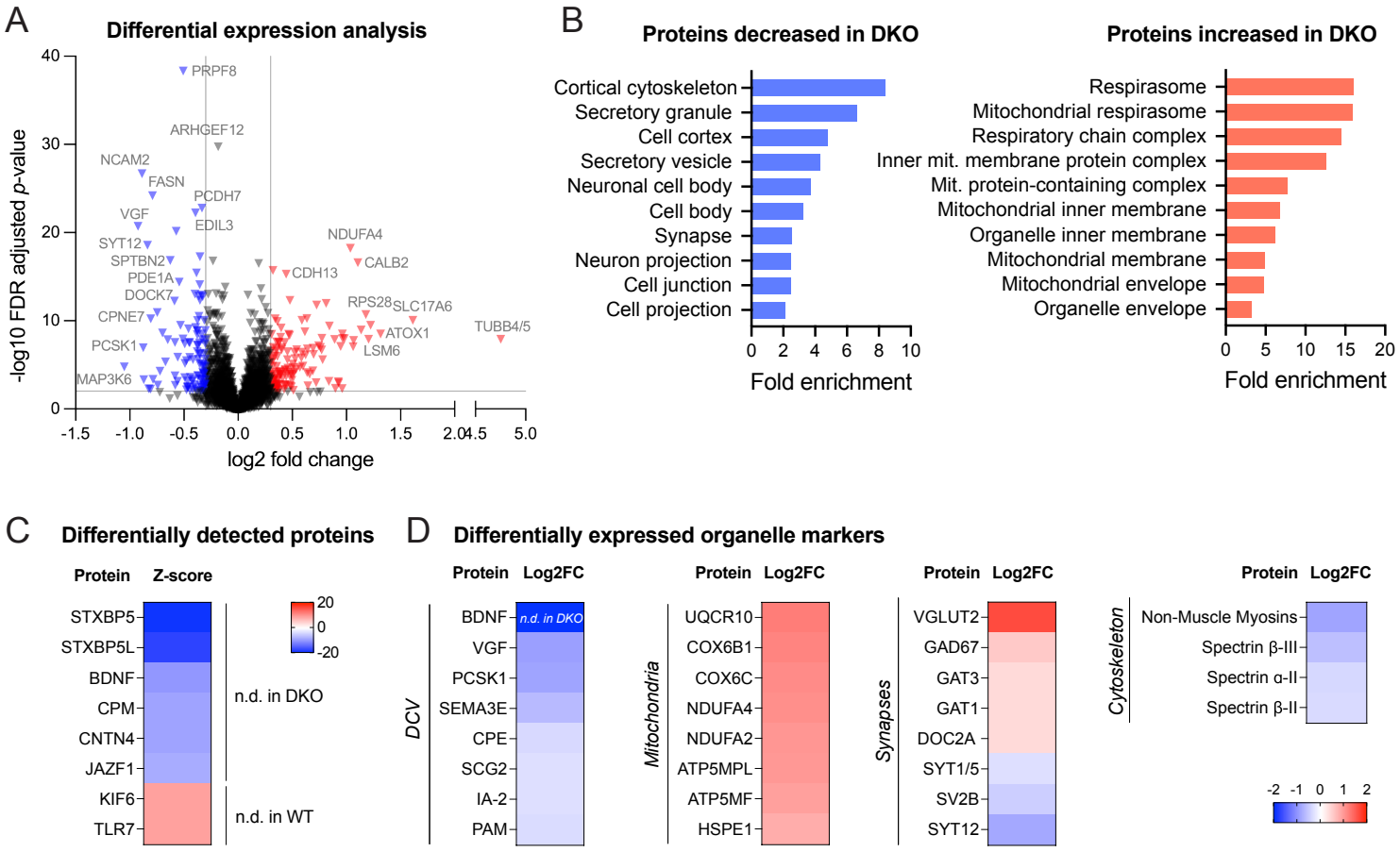
A
Differential expression analysis
-log10 FDR adjusted p-value
log2 fold change
PRPF8
ARHGEF12
NCAM2
FASN
PCDH7
VGF
EDIL3
SYT12
SPTBN2
PDE1A
DOCK7
CPNE7
PCSK1
MAP3K6
NDUFA4
CALB2
CDH13
RPS28
SLC17A6
ATOX1
LSM6
TUBB4/5
B
Proteins decreased in DKO
Cortical cytoskeleton
Secretory granule
Cell cortex
Secretory vesicle
Neuronal cell body
Cell body
Synapse
Neuron projection
Cell junction
Cell projection
Fold enrichment
Proteins increased in DKO
Respirasome
Mitochondrial respirasome
Respiratory chain complex
Inner mit. membrane protein complex
Mit. protein-containing complex
Mitochondrial inner membrane
Organelle inner membrane
Mitochondrial membrane
Mitochondrial envelope
Organelle envelope
Fold enrichment
C
Differentially detected proteins
Protein
Z-score
STXBP5
STXBP5L
BDNF
CPM
CNTN4
JAZF1
KIF6
TLR7
n.d. in DKO
n.d. in WT
D
Differentially expressed organelle markers
Protein
Log2FC
DCV
BDNF
n.d. in DKO
VGF
PCSK1
SEMA3E
CPE
SCG2
IA-2
PAM
Mitochondria
UQCR10
COX6B1
COX6C
NDUFA4
NDUFA2
ATP5MPL
ATP5MF
HSPE1
Synapses
VGLUT2
GAD67
GAT3
GAT1
DOC2A
SYT1/5
SV2B
SYT12
Cytoskeleton
Non-Muscle Myosins
Spectrin β-III
Spectrin α-II
Spectrin β-II

Figure 3

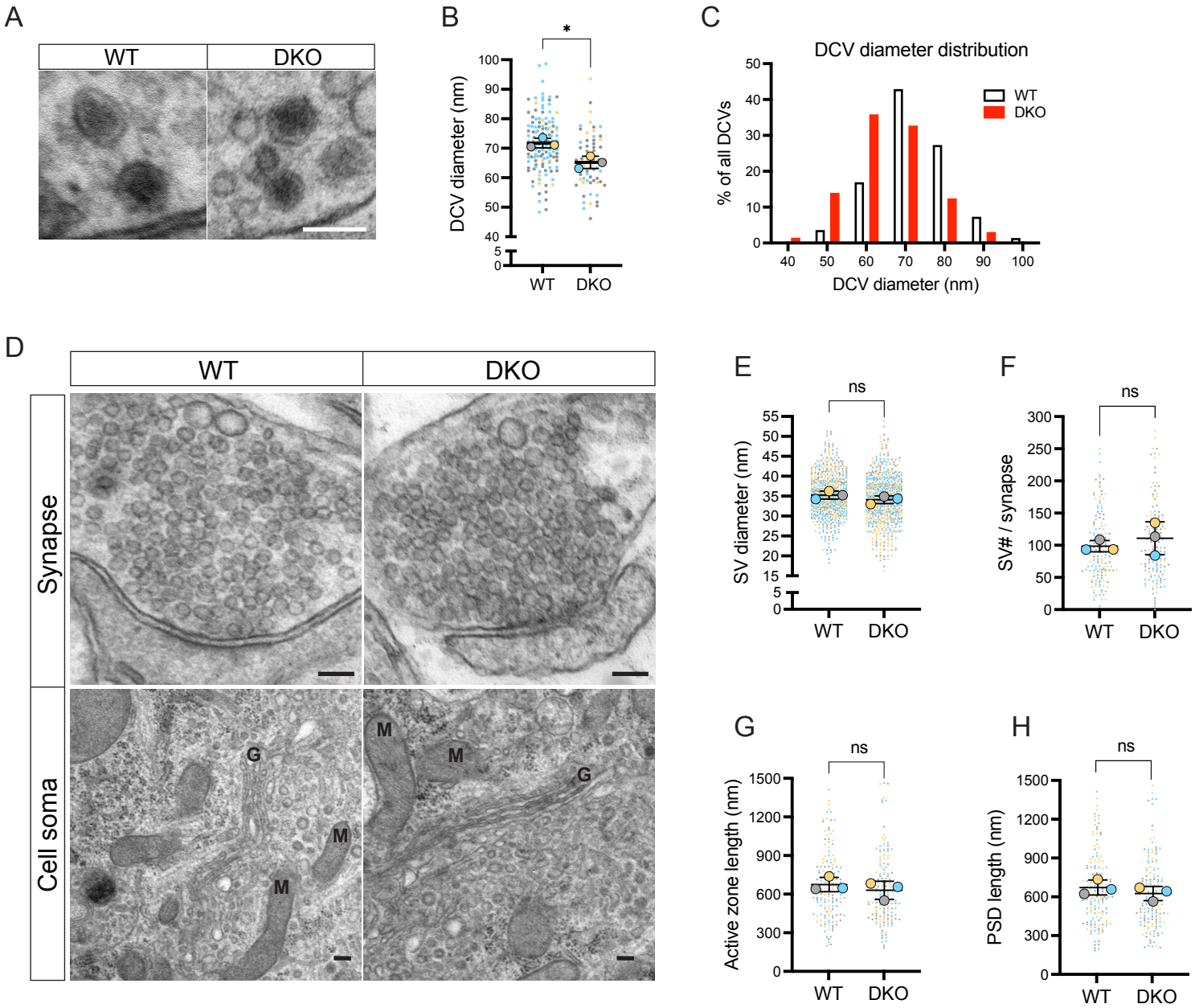
A
WT
DKO
B
*
DCV diameter (nm)
100
90
80
70
60
50
40
5
0
WT
DKO
C
DCV diameter distribution
% of all DCVs
50
40
30
20
10
0
WT
DKO
40
50
60
70
80
90
100
DCV diameter (nm)
D
WT
DKO
Synapse
Cell soma
G
M
M
M
M
G
E
ns
SV diameter (nm)
55
50
45
40
35
30
25
20
15
5
0
WT
DKO
F
ns
SV# / synapse
300
250
200
150
100
50
0
WT
DKO
G
ns
Active zone length (nm)
1500
1200
900
600
300
0
WT
DKO
H
ns
PSD length (nm)
1500
1200
900
600
300
0
WT
DKO

Figure 4

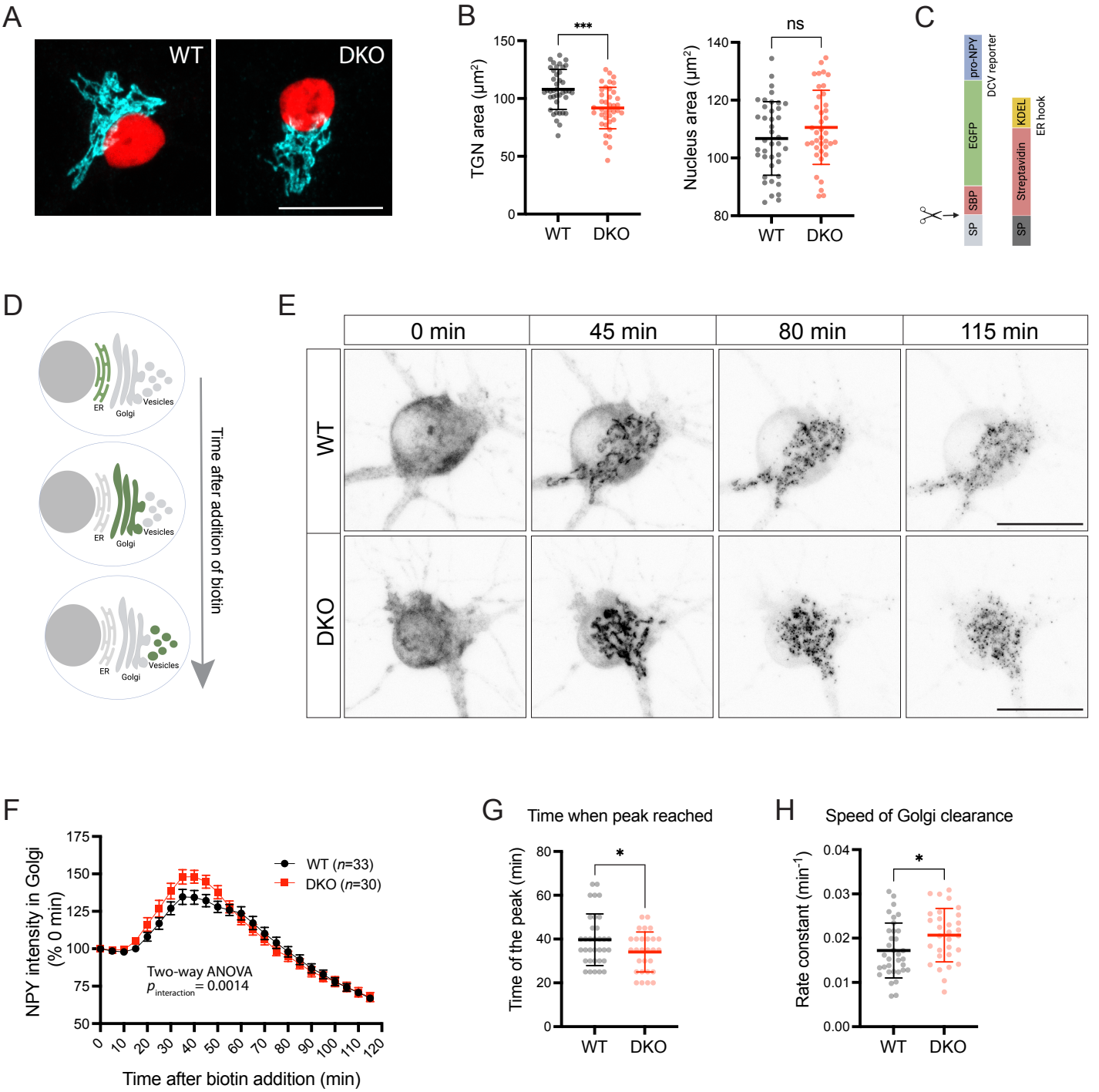
A
WT
DKO
B
TGN area (µm²)
***
WT
DKO
Nucleus area (µm²)
ns
C
pro-NPY
DCV reporter
EGFP
SBP
SP
KDEL
ER hook
Streptavidin
SP
D
ER
Golgi
Vesicles
Time after addition of biotin
E
0 min
45 min
80 min
115 min
WT
DKO
F
NPY intensity in Golgi (% 0 min)
WT (n=33)
DKO (n=30)
Two-way ANOVA
p interaction = 0.0014
Time after biotin addition (min)
G
Time when peak reached
Time of the peak (min)
*
WT
DKO
H
Speed of Golgi clearance
Rate constant (min⁻¹)
*
WT
DKO
I
WT
DKO
J
% anterograde puncta
% puncta
ns
WT
DKO
% retrograde puncta
% puncta
ns
WT
DKO
K
Velocity (anterograde)
Velocity (µm/ sec)
ns
WT
DKO

Figure 5

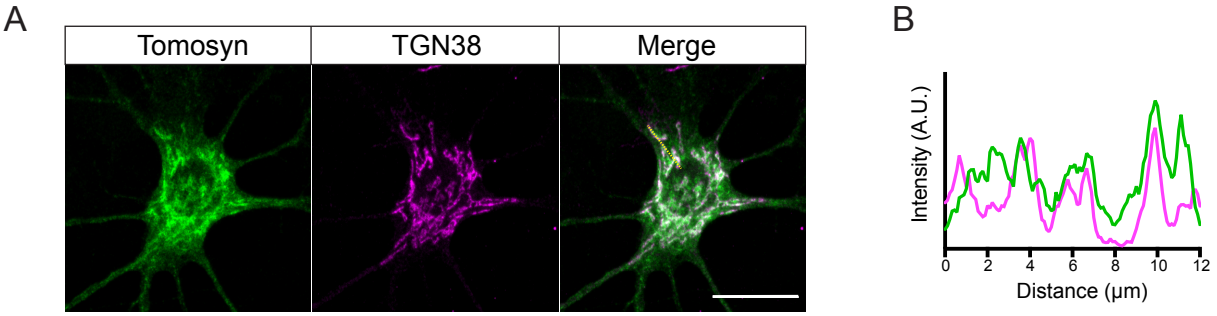

Figure 5–figure supplement 1

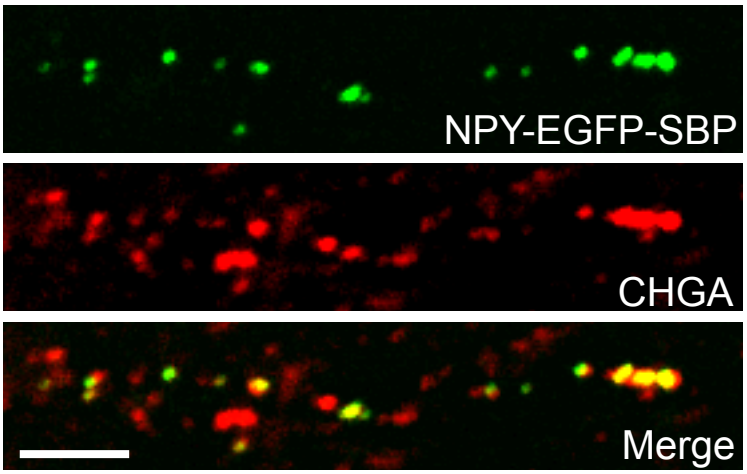

Figure 5–figure supplement 2

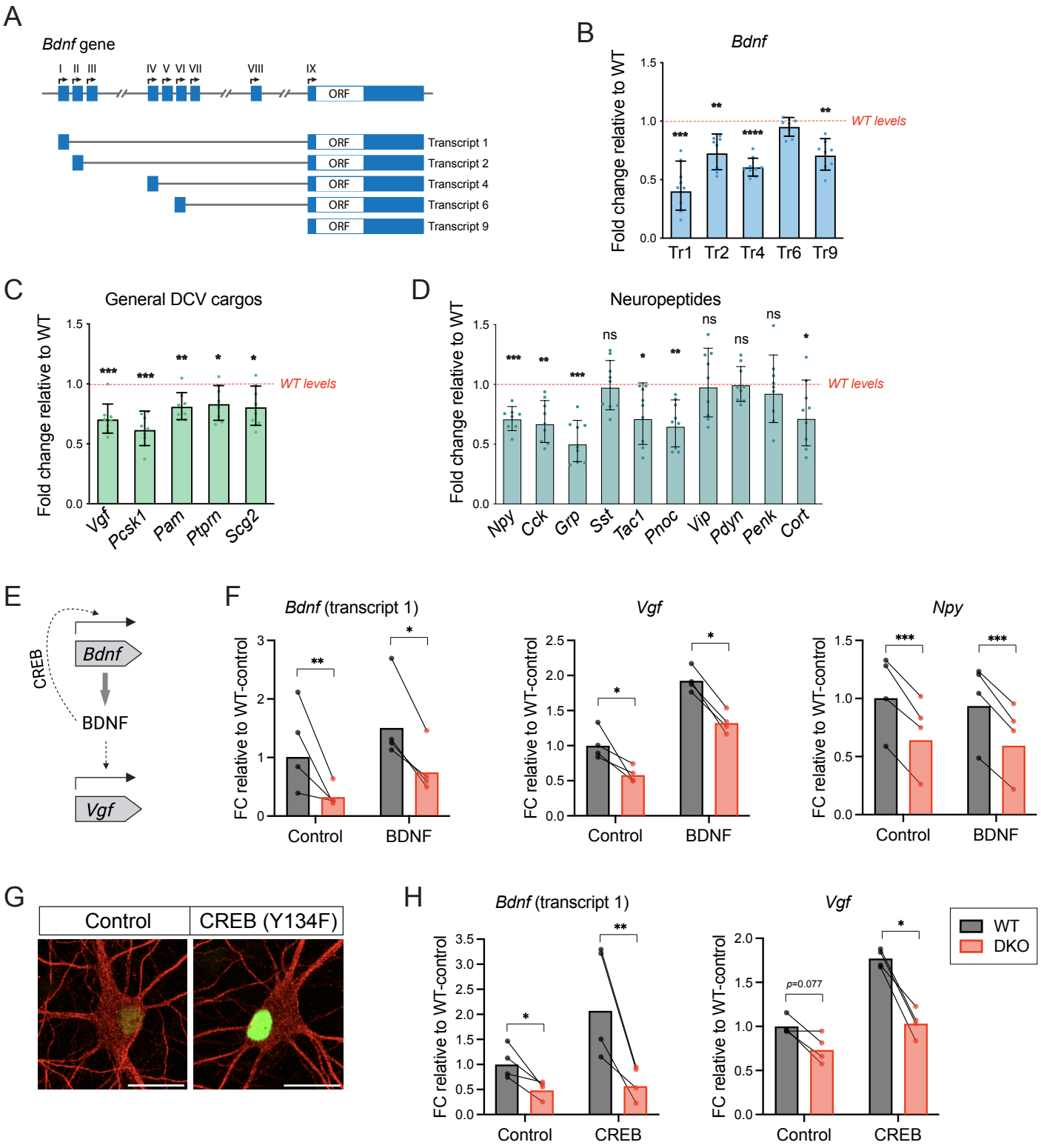
A
Bdnf gene
I II III IV V VI VII VIII IX
ORF
Transcript 1
Transcript 2
Transcript 4
Transcript 6
Transcript 9
B
Bdnf
Fold change relative to WT
WT levels
Tr1 Tr2 Tr4 Tr6 Tr9
C
General DCV cargos
Fold change relative to WT
WT levels
Vgf Pcsk1 Pam Ptprn Scg2
D
Neuropeptides
Fold change relative to WT
WT levels
Npy Cck Grp Sst Tac1 Pnoc Vip Pdyn Penk Cort
E
CREB
Bdnf
BDNF
Vgf
F
Bdnf (transcript 1)
Vgf
Npy
FC relative to WT-control
Control
BDNF
G
Control
CREB (Y134F)
H
Bdnf (transcript 1)
Vgf
FC relative to WT-control
p=0.077
Control
CREB
WT
DKO

Figure 6

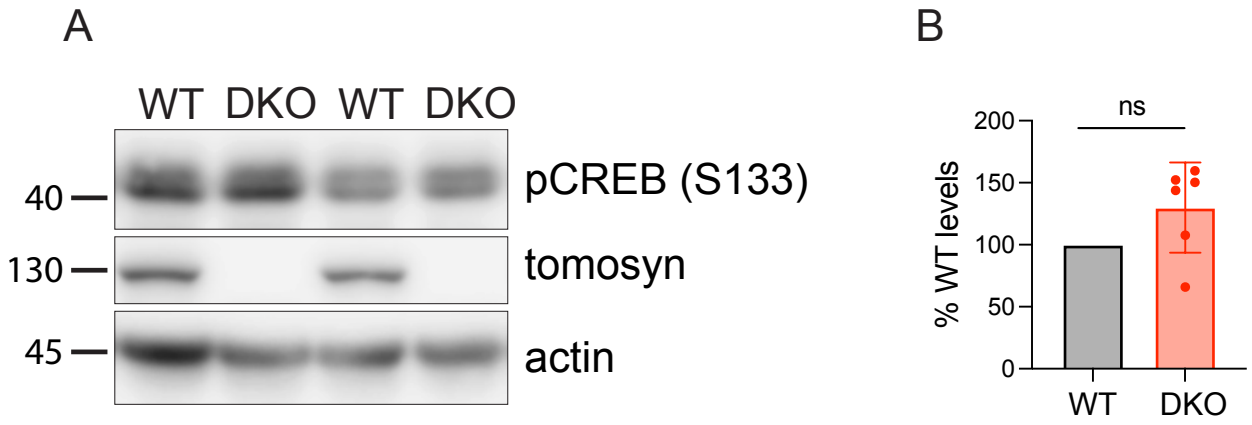

Figure 6–figure supplement 1